Electrophysiogical Evaluation of the Continuity and Transmurality of Surgical Ablation Lesions In Ex Vivo Perfused Porcine Hearts by Unipolar High-Resolution Mapping

K.M. (Kristel) Wenink | Technical Medicine

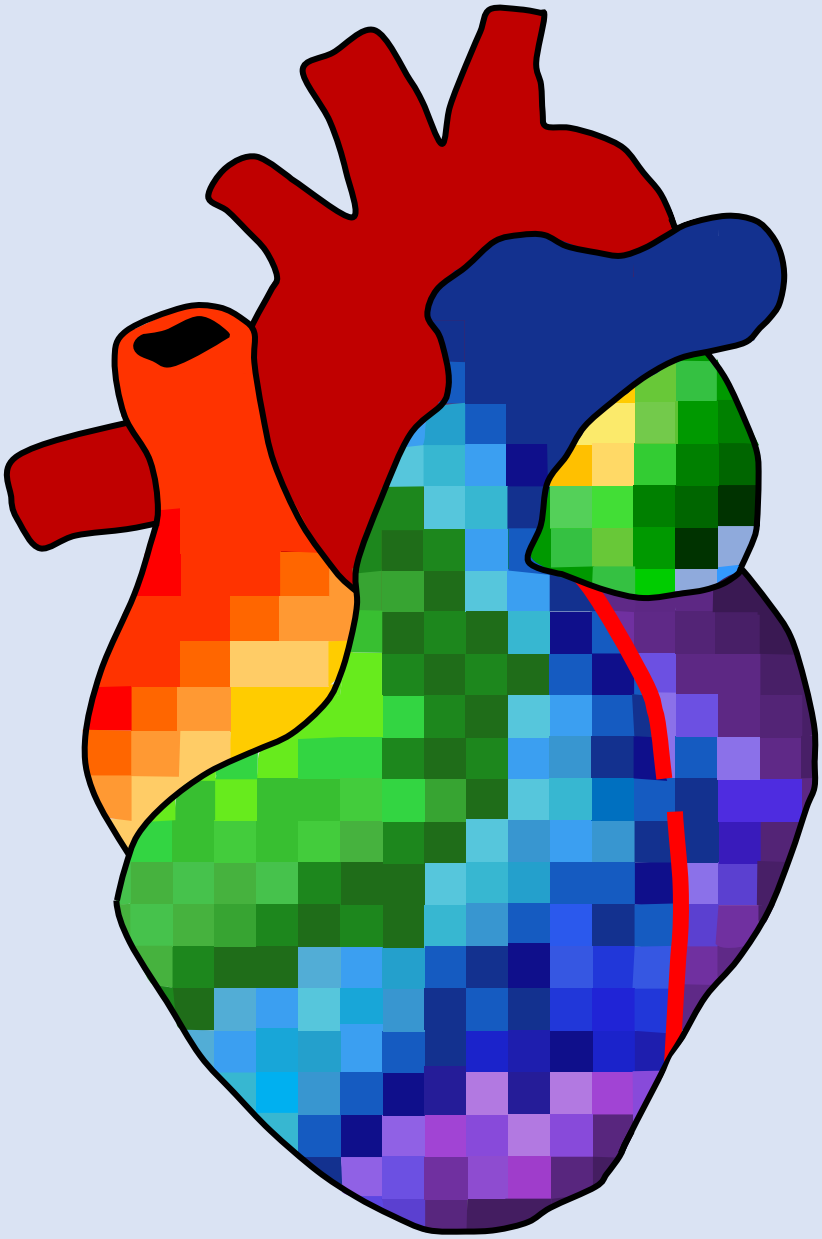

Department of Translational Electrophysiology
Erasmus Medical Center

Electrophysiological Evaluation of the Continuity and Transmurality of Surgical Ablation Lesions in Ex Vivo Perfused Porcine Hearts by Unipolar High-Resolution Mapping

K.M. (Kristel) Wenink
Student number: 4450396
20 March 2023

Thesis in partial fulfillment of the requirements for the joint degree of Master of Science in

Technical Medicine

Leiden University | Delft University of Technology | Erasmus University Rotterdam

Master thesis project (TM30004 – 35 ECTS)
Department of Translational Electrophysiology and Cardiology, Erasmus MC

April 2022 – March 2023

Supervisors

Prof. dr. N.M.S. (Natasja) de Groot	Erasmus MC	Medical supervisor
Drs. M.S. (Mathijs) van Schie	Erasmus MC	Technical supervisor

Thesis committee members

Prof. dr. N.M.S. (Natasja) de Groot	Erasmus MC	Chair and Technical supervisor
Dr. Y.J.H.J. (Yannick) Taverne	Erasmus MC	Medical supervisor
Dr. ir. R.C. (Richard) Hendriks	TU Delft	Independent committee member
Drs. M.S. (Mathijs) van Schie	Erasmus MC	Daily supervisor

Preface

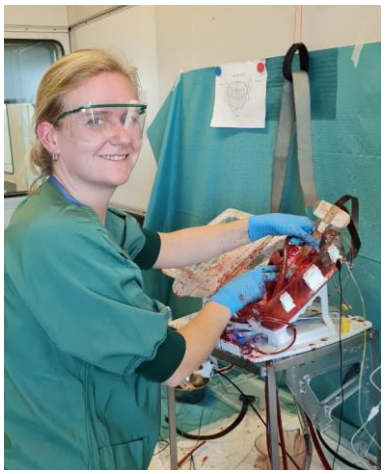

My journey as a Technical Medicine student in Delft started 7.5 years ago. It had been a big quest to find out what I wanted to study, mainly because I had too many interests. I attended open days for a wide variety of majors, from mathematics to psychobiology, even Greek and Latin. After careful consideration, I decided on Technical Medicine, as the degree seemed very versatile due to the combination of medical, social, and technical aspects. Three fun years flew by. After a gap year, during which I worked as a general practitioner's assistant for half a year and traveled through Southeast Asia and South Africa for half a year, I started the master track Sensing and Stimulation. Today, 7.5 years later, I can confidently say that Technical Medicine was the right choice for me. I did not enjoy all aspects of the internships, but they taught me a lot about myself and my interests. It has been confirmed over and over again that the topics that interested me the most were the ones where medicine and engineering meet. During my first internship in the department of Cardiology and Translational Electrophysiology, I was impressed by the research on thousands of cardiac signals measured during cardiac surgery or on ex vivo perfused porcine hearts. I had to come back!

I would like to thank my supervisors Natasja de Groot and Mathijs van Schie. Natasja, thank you for welcoming me back to your research department and for taking time out of your busy schedule to share your knowledge and enthusiasm with me. Your positivity, passion, and the way you manage the department inspires me. Mathijs, thank you for always having your door open for all my questions, for your positivity, your valuable feedback and for taking away my worries in stressful times. Yannick Taverne, my research on ex vivo perfused porcine hearts would not have been possible without you and your team. I want to thank you for that and for being part of my graduation committee. Richard Hendriks, thank you for being part of my graduation committee. Thank you to all my colleagues in the research department who made my time so enjoyable and were always willing to share their knowledge with me. My special thanks to the ex vivo heart perfusion team who helped me with the ablation experiments. Hongxian, thank you for our collaboration and brainstorm sessions during my master's thesis. Finally, I would like to thank my family and friends for always supporting me and making my time as a student unforgettable. I now bid farewell to my chapter as a student and look forward to all that the future holds.

K.M. Wenink

Rotterdam, March 2023

Abstract

Introduction: Currently, there is no method available for intra-operative evaluation of the completeness (transmurality and continuity) of surgical ablation lesions. This study aimed to investigate the changes in electrogram characteristics and activation patterns caused by different (non)transmural and (dis)continuous ablation lesions in ex vivo perfused porcine hearts.

Methods: Donation after circulatory death porcine hearts ex vivo perfused in Langendorff mode were used to perform ablation experiments in a controlled setting. Three subsequent radiofrequency ablation lesions – with different degrees of transmurality and continuity - were created on the right ventricle using AtriCure's Isolator Synergy Bipolar clamp. Electrograms of the lesion and surrounding tissue were recorded by unipolar high-resolution mapping. These measurements were executed during pacing perpendicular to the ablation lesion from two sides and during intrinsic cardiac rhythm. Electrograms were processed using custom-made software. The inter-electrode conduction time, potential voltage, potential slope, and R-to-S-amplitude ratio were analyzed.

Results: The first radiofrequency application significantly affected all parameters in the lesion area. Conduction times increased, the potential voltage and slope decreased, and there was a loss of S-wave amplitude. The increase in conduction time and the decrease in voltage were less steep when there was a conduction gap in the ablation line. However, conduction time was less sensitive to lesion transmurality because it remained stable even when the lesion became more transmural. The potential voltage on the other hand, became significantly lower in transmural lesions, showing an overall decrease of 84% from baseline to the third (complete) lesion. The potential slope showed similar trends as the voltage, although it was less discriminative for (non)transmurality and (dis)continuity. The loss of the S-wave became significantly more pronounced with more radiofrequency delivery.

Conclusions: Complete ablation lesions are characterized by a stable conduction time when applying subsequent ablation, a decrease in potential voltage of 84% on the lesion and its border zone, and loss of the contribution of S-wave amplitude. The combination of these parameters in one tool could help to detect incomplete surgical ablation lesions in the individual patient during Maze surgery. This could potentially reduce post-maze gap-related atrial tachyarrhythmias and thus improve long-term success rates.

List of Abbreviations

AAD	Antiarrhythmic drugs
ABC	Atrial Fibrillation Better Care
AF	Atrial fibrillation
AT	Atrial tachyarrhythmia
CT	Conduction time
DCD	Donation after circulatory death
DP	Double potential
EGM	Electrogram
EMC	Erasmus Medical Center
EP	Electrophysiology
EVHP	Ex vivo heart perfusion
IQR	Interquartile range
IVC	Inferior vena cava
LA	Left atrium
LV	Left ventricle
PV	Pulmonary vein
RA	Right atrium
RF	Radiofrequency
RV	Right ventricle
SVC	Superior vena cava

Table of contents

Introduction

Atrial fibrillation (AF) is a common cardiac arrhythmia and therapy options include pharmacological or electrical cardioversion, antiarrhythmic drugs (AAD), catheter ablation, or surgical ablation [1]. Surgical ablation, also known as the Maze procedure, is considered in patients in whom cardioversion, AAD, and catheter ablation previously failed, who are at high risk of catheter ablation failure, or who undergo cardiac surgery for other reasons [1-4]. During Maze surgery, multiple ablation lesions are created in the cardiac tissue to block the abnormal electrical signals that cause AF [1-3]. The success rate of Maze surgery is higher than catheter ablation, as the freedom from atrial arrhythmias at 1 year is 78% to 92% [5, 6] versus 40% to 73% [7-11], respectively. Also, a meta-analysis of three randomized controlled trials showed significantly higher freedom from atrial tachyarrhythmias (ATs) and less need for redo procedures after surgical ablation compared with catheter ablation for paroxysmal or persistent AF [12]. However, surgical ablation is more invasive, with higher complication rates and longer hospitalization [12, 13], and therefore it seems reasonable to consider surgical ablation only in a selected group of patients [1].

To ensure the success of ablation procedures and prevent the recurrence of AF or other ATs, the ablation lesion must be complete, i.e., the ablation lesion must be 1) continuous (without any gaps that enable electrical conduction) and 2) transmural (extending through all myocardial layers). Despite the high success rate of the Maze procedure, some patients still experience recurrent atrial arrhythmias, mostly due to incomplete lesion lines [14-17]. These patients may be candidates to undergo an electrophysiology (EP) study and catheter ablation post-maze surgery, to resolve the recurrent arrhythmia [3]. The incidence of ATs after the Maze procedure was reported to be 5-15% [18]. Two retrospective studies by Gopinathannair et al. (2017) [18] and Suzuki et al. (2021) [17] show similar results on the origins and nature of post-maze ATs. Macro-reentry circuits were reported to be the most common cause of post-maze ATs, accounting for 70-75%. Of these, roughly two-thirds are of a left-sided origin, which was in line with other previous studies [19-21]. Of these left-sided macro-reentry ATs, the predominant circuits are peri-mitral atrial flutter and left atrial (LA) roof-dependent atrial flutter. In right-sided origins, peri-tricuspid atrial flutter was the most common. Additionally, Suzuki et al. (2021) [17] showed that 81.6% of all post-maze ATs were gap-related.

This highlights the difficulty of ensuring a complete ablation line during the initial procedure and emphasizes the importance of finding and ablating conduction gaps in lesion lines for a successful ablation outcome [22-24]. An intra-operative electrophysiological evaluation method could fulfill a key role in identifying and addressing incomplete lesion lines during the initial Maze procedure. However, such a method is currently unavailable for surgical ablation procedures, and research in this area is limited.

There have been significant advances in the methods used to evaluate the completeness of catheter ablation lesions at the EP laboratory. These methods include assessing the presence of double potentials (DP), entrance and exit block, and lower voltages in ablated areas, as

described in my systematic review titled "Electrophysiological Evaluation of the Continuity and Transmurality of Catheter Ablation Lesions in Atrial Fibrillation Patients: A Systematic Review" [25]. Principles from the electrophysiological evaluation at the EP laboratory can partially be translated for the development of a surgical evaluation tool. However, whereas catheters only give access to ablate and measure the endocardium, the epicardium is also exposed during cardiac surgery. This provides us with more possibilities and information for an accurate evaluation and might provide new insights. Furthermore, the endovascular approach deployed at the EP laboratory raises more limitations in electrode dimensions and resolution as compared to cardiac surgery, which can also impact electrogram (EGM) characteristics [26].

Ex vivo perfusion porcine hearts provide the optimal, controlled setup to investigate the electrophysiological characteristics of different types of surgical ablation lesions. This will be the foundation for the development of an intra-operative high-resolution mapping approach to evaluate surgical ablation lesions. This way incomplete lesion lines can be identified and addressed during the initial procedure, potentially reducing the need for additional catheter ablation procedures and improving the long-term success of the Maze procedure in preventing AT recurrence. New insights might also be valuable for the EP laboratory.

Master's thesis objective and outline

The goal of my master's thesis is to quantify electrophysiological characteristics of ablation lesions and conduction gaps using unipolar high-resolution mapping data from experiments on ex vivo perfusion porcine hearts (Langendorff model). This will be the foundation for the development of a novel intra-operative mapping approach to evaluate surgical ablation lesions. This work builds upon the existing knowledge and techniques for evaluating catheter ablation lesions, as outlined in my systematic review [25]. This results in the following (sub-)goals for my master thesis:

1. Set up and execute ablation experiments on ex vivo perfusion porcine hearts.
2. Process acquired data with custom-made software to identify local electrical activity.
3. Identify which electrogram characteristics or activation patterns are associated with nontransmural and/or discontinuous ablation lesions.
4. Translate the results on ex vivo perfusion porcine hearts to clinical data obtained during Maze surgery.

Background

Atrial fibrillation

AF is a common cardiac arrhythmia characterized by rapid and unorganized activation of the atria with an irregular ventricular response [27, 28]. The chances that one develops AF during its lifetime is 25% above the age of 40. These chances increase significantly with age, making it the most prevalent arrhythmia developed with age, a "disorder of the elderly" [4, 29-33].

Prevalence in the Netherlands has increased in recent years, from 0.4% of the total population in 2008 to 1.4% in 2017. In people aged 85 years and older an increase took place from 6 to 16% [34]. 70% of the afflicted persons are between the ages of 65 and 85 with a median age of diagnosis of 75 years. The aging of the population and improved outcomes of many chronic medical conditions have led to increases in AF diagnoses [4]. However, the increase may partly be due to improved registration of AF. Nonetheless, the numbers show that the prevalence of AF is of considerable significance [34].

Even though AF is not considered a life-threatening arrhythmia, it is independently associated with increased morbidity and mortality. It is known to be associated with an increased risk of transient ischemic attacks, ischemic stroke (five times higher [1, 32]), systemic embolism, and all-cause mortality (1.5-1.9 times higher [30]). Risks are increased in populations with preexisting cardiovascular comorbidities [4, 32, 33], but also by certain reversible causes like hyperthyroidism, unhealthy alcohol use, and obesity [35].

Mechanisms of AF

The stage of AF is classified according to its duration and length of episodes, as described in the 2014 American Heart Association/American College of Cardiology/Heart Rhythm Society guidelines: 1) paroxysmal (terminates spontaneously within seven days); 2) persistent (fails to self-terminate within seven days); 3) long-standing persistent (lasted for more than 12 months) and 4) permanent (if a patient and clinician made a joint decision to not treat the persistent AF anymore) [1, 28, 35, 36].

AF and its stage are the results of a complex interplay between triggers (focal or reentry activity responsible for the initiation of AF) and arrhythmogenic substrate (responsible for the perpetuation of AF) [28, 37]. Tissue remodeling results in a substrate that perpetuates AF. Atrial remodeling can either be 1) electrical (AF induces transient changes in atrial electrophysiology, like a decrease in atrial refractoriness and altered expression and function of ion channels, that promote its perpetuation, indicating that AF begets AF [28, 37-39]) or 2) structural (most importantly due to fibrosis, but also fatty infiltration, inflammatory infiltration, and necrosis [28, 37]). The most common site for triggers is in the pulmonary veins (PV) [3, 24, 37, 40, 41]. Early in the course of AF, the atrium is relatively healthy and therefore contains a small degree of an arrhythmogenic substrate, and as a result, AF terminates spontaneously. As the tissue remodels further over time, leading to a substrate for perpetuation, AF no longer terminates spontaneously and

becomes persistent [3, 37]. This illustrates the progressive nature of AF through a long-term positive feedback loop, and therefore, early interventions, before irreversible remodeling, are of major importance. Many triggers but little substrate mean short AF episodes (paroxysmal AF). Much substrate results in the perpetuation of AF ((longstanding) persistent AF), and a single trigger may be enough to initiate it.

Treatment of AF

The ABC-pathway

A useful framework for the general care of AF patients is the ABC (Atrial Fibrillation Better Care) pathway, where the 'A' stands for Anticoagulation/avoid stroke; the 'B' for Better symptom management; the 'C' for Cardiovascular and Comorbidity optimization [1, 35].

AF management may consist of antithrombotic therapy to prevent stroke, rate or rhythm control, and lifestyle changes. Rate control consists of the administration of drugs aimed at lowering the heart rate, which is often sufficient to improve AF-related symptoms. Rhythm control is the attempt to restore and maintain sinus rhythm. This may be achieved by a combination of treatment approaches, including electrical and pharmacological cardioversion, antiarrhythmic medication, and catheter ablation [1, 7, 23, 24, 35, 40-46]. In a selected group of patients surgical ablation, also known as the Maze procedure, is considered.

Maze surgery

Maze surgery is considered in patients in whom catheter ablation previously failed, who are at high risk of catheter ablation failure, or who undergo cardiac surgery for other reasons [1]. The Maze procedure, developed in the 1980s, aims to create a "maze" of functional myocardium within the atrium that allows for the propagation of atrial depolarization while reducing the likelihood that the wavefront would promote micro re-entry. The maze is brought about by creating a pattern of scars [1-3]. The most commonly performed procedure is referred to as the Cox-Maze IV and it consists of a pattern of linear scars. Traditionally, lines of scar were made with several small incisions, which is referred to as the "cut and sew" technique. With the introduction of cryothermal and radiofrequency (RF) ablation, this transferred to creating lines of scar with ablative technology. Follow-up demonstrated that not all of these ablative techniques resulted in transmural lesions [47, 48]. Practically, however, it was demonstrated that the Maze procedure with the cut and sew technique could be replaced by the more sophisticated ablative techniques that are also technically less demanding [2]. This way the procedure could be simplified and shortened, so the "cut and sew" technique became less frequently utilized and is now rarely performed [2, 3].

The constructed ablation lesions developed over time and the Cox-Maze IV procedure is now considered the golden standard. This procedure includes on the LA a box lesion (isolating the four PVs and the LA posterior wall), which is then connected to the mitral valve annulus and the left atrial appendage. Additionally, the left atrial appendage is removed. In the right atrium (RA) an ablation line from the superior vena cava (SVC) to the inferior vena cava (IVC) is created and an ablation line along the right atrial free wall down to the tricuspid annulus [2, 3]. For an overview of the ablation lines, see Figure 1.

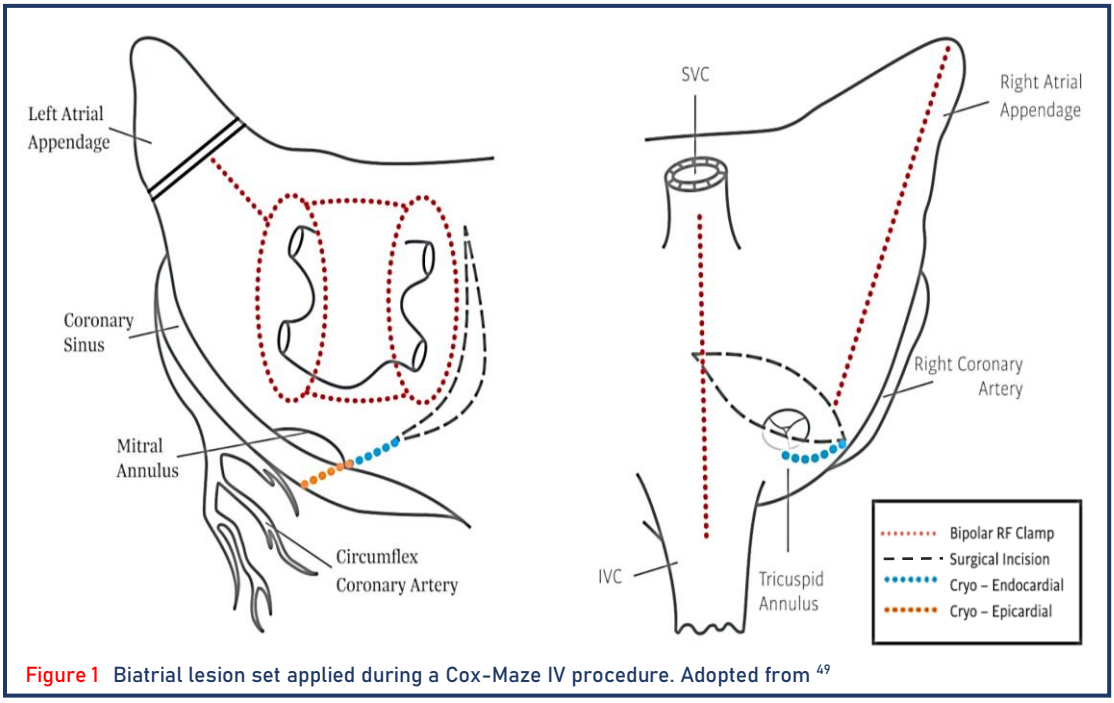

Figure 1 Biatrial lesion set applied during a Cox-Maze IV procedure. Adopted from [49]

Not all patients who undergo Maze concomitant to cardiac surgery undergo a full Cox-Maze IV. Sometimes another lesion set is deemed more appropriate. There is still no clear evidence on which is the most appropriate lesion set and which patients benefit most from either a left atrial-only approach versus a biatrial approach. The decision of the lesion set depends on factors like the frailty of the patient, the severity of AF, and the planned cardiac surgery. Some surgeons advocate a left atrial-only approach during surgery where only the LA is open (e.g. mitral valve repair). While the Maze procedure can be performed during cardiac surgery using a sternotomy, it has also been performed through a minimally invasive approach or video-assisted thoracic surgery [2, 3].

The surgical approach to treat AF has a high success rate. A single-center study of 853 patients who underwent the Cox-Maze IV reported freedom from any AT of 92%, 84%, and 77% at 1, 5, and 10 years respectively. The majority of the patients were treated for nonparoxysmal AF [5]. Another study of 100 patients undergoing Cox-Maze IV for lone persistent AF reported 84% freedom from AF and AAD at 2 years [50]. Another study of 282 AF patients undergoing Cox-Maze IV reported a 78% freedom of AF and AAD at 1 year [6]. In an observational study by Hen et al. (2015) [51] 576 patients underwent the Cox-Maze IV procedure. Overall, 78 percent experienced freedom from AF at five years and 66 percent were free from AF without the use of AAD. There was no difference found between patients with paroxysmal AF and (longstanding-)persistent AF. Results of these studies should be interpreted with caution due to heterogeneity in cohorts (e.g. is the use of AAD allowed, different stages of AF, different underlying comorbidities).

Ex vivo heart perfusion

Ex vivo heart perfusion (EVHP) is a technique that restores the contractile and electrical functions of the heart outside of the body by providing mechanically supported warm circulation, resulting in a beating heart [52]. In the clinical context, EVHP has emerged as a promising technique to expand the donor pool for heart allografts. This is of great importance as demand for donor hearts exceeds its supply due to the increasing number of patients with

end-stage heart failure. EVHP facilitates extended duration of organ preservation, extended transport times, and extended criteria for donor hearts. Until recently, donation after brain death donors were the only donors eligible for heart transplantation. Donation after circulatory death (DCD) donors were previously not considered due to issues of unquantifiable warm ischemic injury to the myocardium and the inability to assess cardiac function in the asystolic heart. However, EVHP shows promising results for the inclusion of DCD donors by allowing assessment and optimization of cardiac function after explantation and before implantation [53, 54]. In the field of research, EVHP provides the ideal setup to study cardiac parameters such as contractility and cardiac electrical activity under controlled conditions. The two main methods to perfuse isolated hearts are the Langendorff model and the Working heart model. The research unit of Translational Electrophysiology deploys the Langendorff model. In Figure 2 the setup and blood flow of the Langendorff system are shown. The Langendorff system relies on retrograde perfusion of the heart. The aorta is cannulated and retrogradely perfused by a perfusion pump, allowing perfusion of the coronary vasculature. This way the heart is provided with oxygen and nutrients through the coronary arteries. Since the aortic valve allows blood to flow in only one direction, from the left ventricle (LV) to the aorta, the perfusate does not enter the LV. However, a vent is positioned in the LV through a PV to relieve the LV of any blood that might leak into the LV in case of aortic insufficiency. The venous return from the heart is collected in the cardiac veins, which eventually all come together in the coronary sinus. The coronary sinus delivers the deoxygenated blood back to the RA, after which it enters the right ventricle (RV). This means that in the Langendorff model, the right side of the heart is perfused, as opposed to the left side [52].

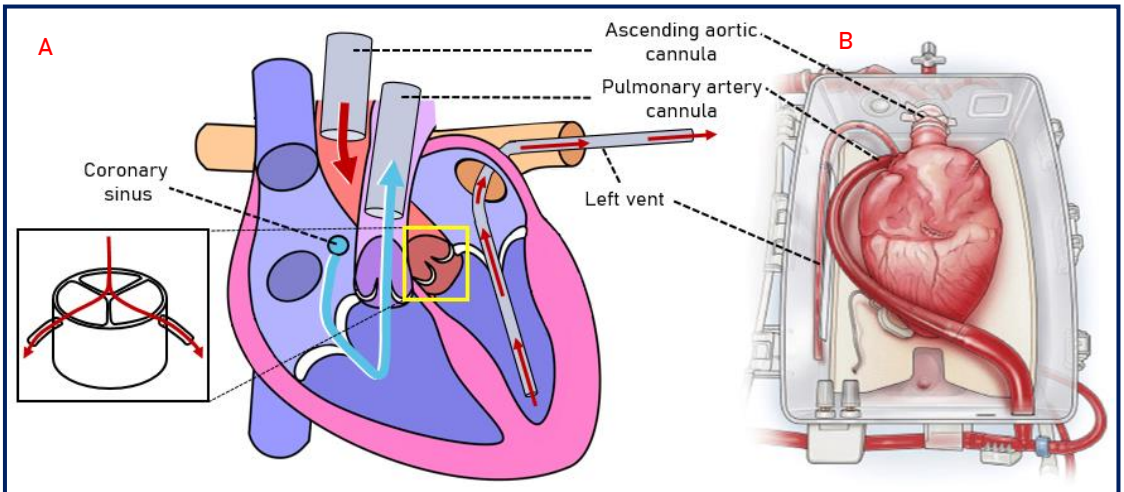

Figure 2 EVHP setup according to Langendorff. A) Direction of blood flow during retrograde perfusion of the heart. The perfusion fluid enters the aorta via the inserted cannula. Because the aortic valve allows only unidirectional blood flow, the perfusate does not enter the LV, but flows only into the coronary system, whereupon the venous return returns to the RA via the coronary sinus. The perfusate exits the heart through the cannula inserted into the pulmonary artery. A left vent is inserted through a pulmonary vein to relieve the LV of any blood leakage due to possible aortic insufficiency. The IVC and SVC are ligated; B) The heart positioned in the perfusion setup. The heart is viewed from the posterior side. *EVHP = ex vivo heart perfusion; LV = left ventricle; RA = right atrium.; IVC = inferior vena cava; SVC = superior vena cava.*

Methods

Ex vivo perfused porcine hearts

The study included DCD porcine slaughterhouse hearts on EVHP. Data was acquired through ablation experiments conducted at the research unit of Translational Electrophysiology at the Erasmus Medical Center (EMC), between October and December 2022.

Outline of the experimental protocol

In the first phase of my master's thesis, I developed an experimental protocol to acquire electrophysiological data on different stages of ablation lesions. The protocol consisted of four phases, see Figure 3. At first, a baseline measurement was recorded prior to ablation, following a predefined mapping scheme. After baseline measurements, three different levels of RF ablation lesions were subsequently created at the same RV site. This way, different degrees of transmurality and continuity of the lesion are established. After each lesion, the same mapping scheme was repeated.

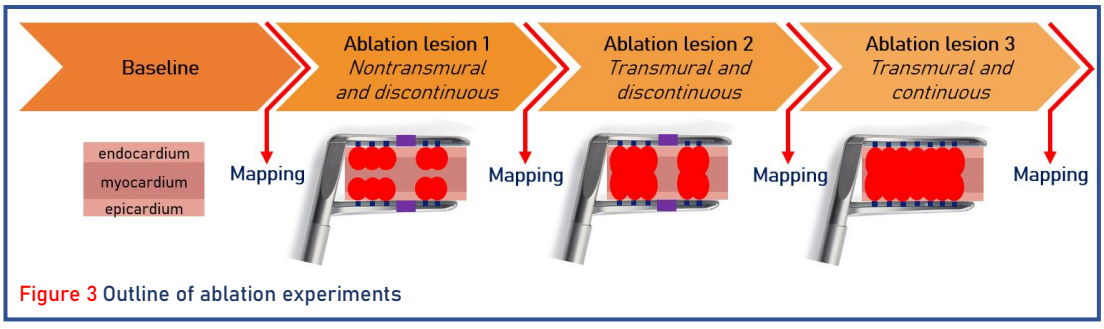

Figure 3 Outline of ablation experiments

Ex vivo heart perfusion setup

For every experiment, hearts are excised and blood collected as per standard procedure at the slaughterhouse. After excising the heart, a cardioplegic solution is administered, to limit the warm ischemic time. The heart is placed on ice and transported to the laboratory for EVHP. At the laboratory, cannulas were fixed in the ascending aorta and pulmonary artery, caval veins were closed off, and a vent was positioned in the LV through a PV (Figure 4). The heart was reperfused in Langendorff model (coronary flow 750 to 850 ml/min) with a mixture of priming solution and porcine blood, subsequently leading to active coronary perfusion and spontaneous contractions [55].

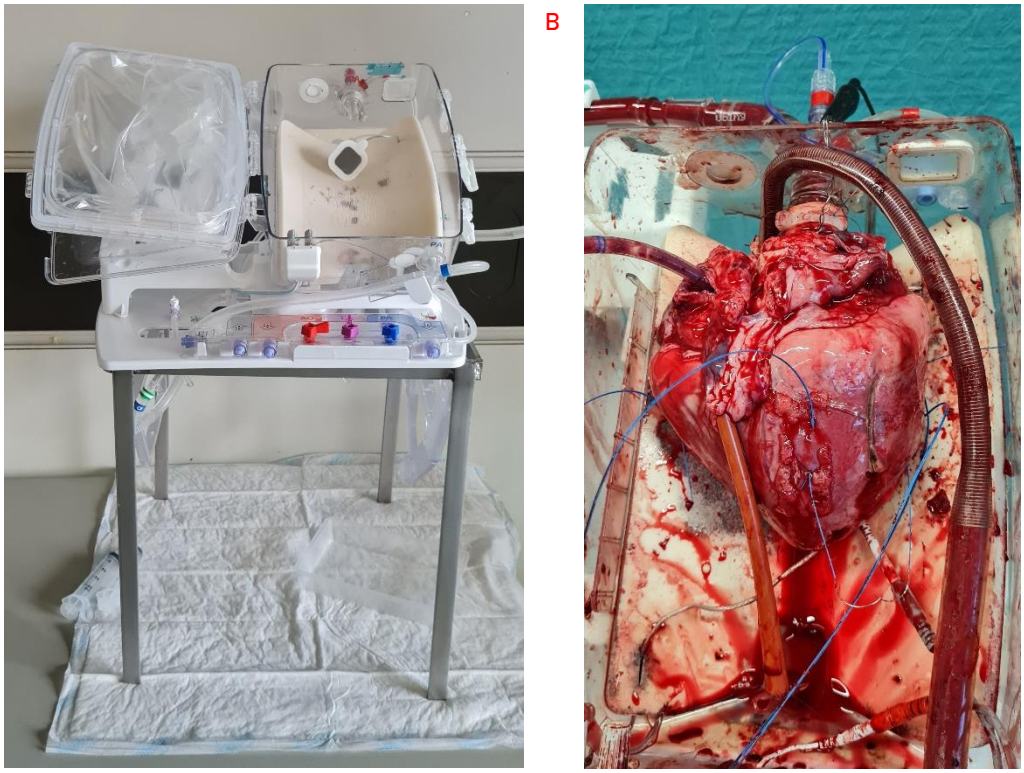

Figure 4 Ex vivo heart perfusion (EVHP) setup. EVHP allows to reperfuse excised hearts and research them in a beating state. A) The heart perfusion set; B) Placement of porcine heart within the ex vivo perfusion model.

Ablation

AtriCure's Isolator Synergy Ablation System

AtriCure's Isolator Synergy Bipolar clamp in combination with the AtriCure Ablation and Sensing Unit (ASU), AtriCure Switch Matrix (ASB), and footswitch was used to perform RF ablation throughout the experiment, see Figure 5. The ablation clamp uses dual electrodes with alternating and overlapping fields to form a lesion from the middle of the myocardium to the surface. The jaws of the clamp are closed upon ablation and they maintain consistent pressure on the tissue throughout ablation. During ablation, a monitoring algorithm measures the tissues' response to RF delivery, based on tissue conductance between the electrodes, 50 times per second. Accordingly, the energy output and ablation time are adjusted [56].

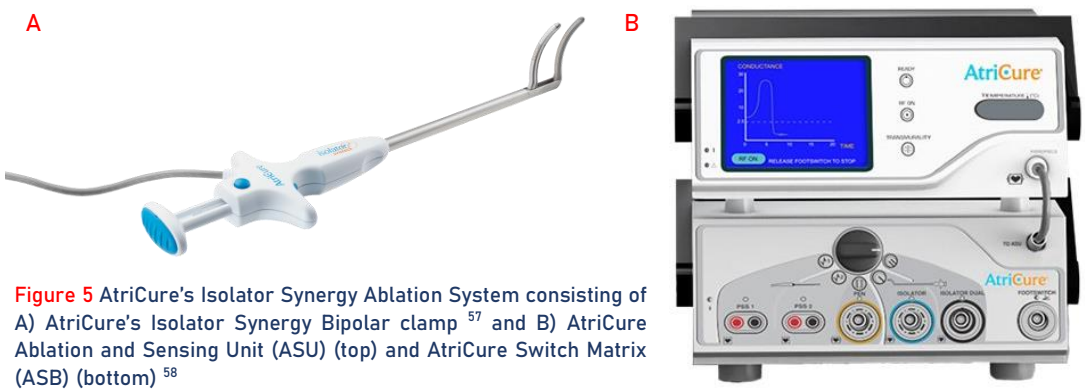

Figure 5 AtriCure's Isolator Synergy Ablation System consisting of A) AtriCure's Isolator Synergy Bipolar clamp [57] and B) AtriCure Ablation and Sensing Unit (ASU) (top) and AtriCure Switch Matrix (ASB) (bottom) [58]

Ablation settings

The settings for lesion creation were based on the ablation settings that are used in the operation room in the EMC during Maze surgery. AtriCure's ASU measures the conductance in millisiemens (mS) (inverse of impedance) of the tissue being treated, see Figure 6. Ablation starts when pushing the footswitch and will automatically stop after 40 seconds of application, or the surgeon manually stops when conductance drops below 2.5 mS, after which AtriCure states the lesion is transmural. In clinical practice, to ensure a complete lesion, the surgeon will repeat this process until the conductance falls below 2.5 mS within 5 seconds. This guideline is somewhat arbitrary and it is at present unknown which settings ensure a transmural and continuous lesion.

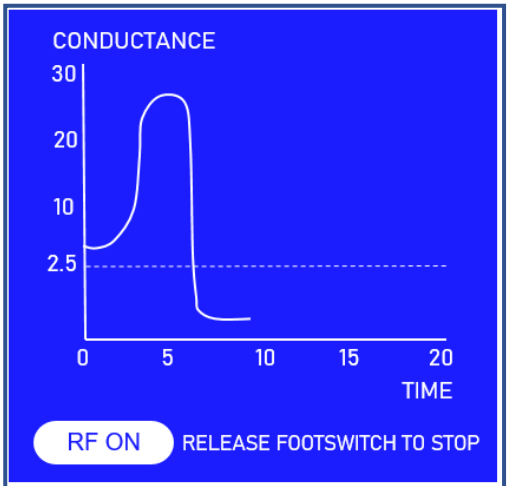

Figure 6 Conductance measurement during ablation, depicted on AtriCure's Ablation Sensing Unit (ASU).

Lesion location

For practical reasons, the experiment was executed on the RV instead of the atria. This was done because, usually, the atria did not restart after reperfusion of the heart. Given the fact that the atrial wall is thinner than the ventricular wall, the RV was selected over the LV, as it has the thinner myocardial wall of the two ventricular chambers. An incision on the RV lateral wall was created to insert the ablation clamp, see Figure 7.

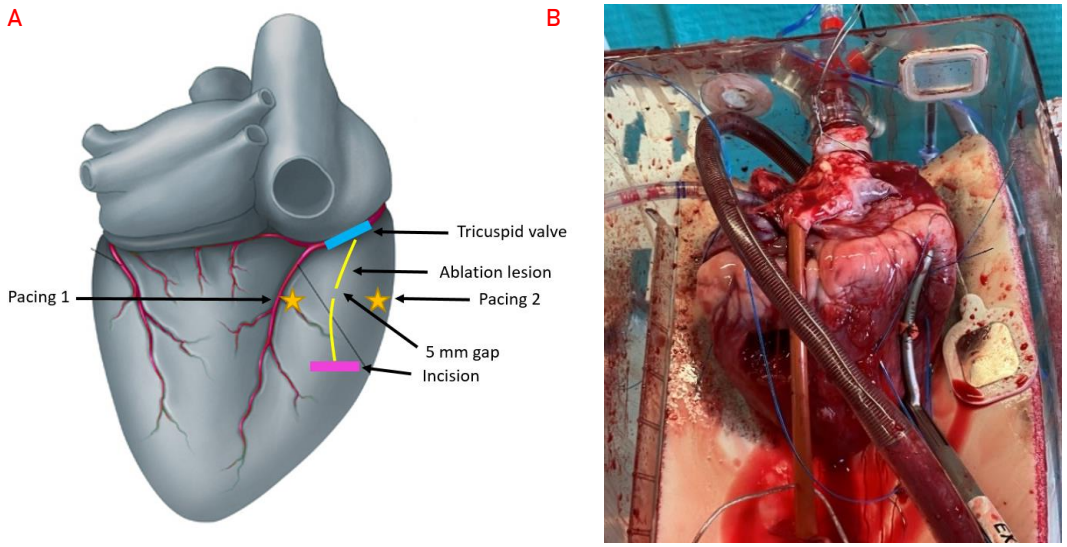

Figure 7 A) Schematic overview of the location of the ablation lesion on the right ventricle, the intentional conduction gap, and the pacing locations; B) The surgical ablation clamp inserted through the incision to create the ablation lesion on the right ventricle.

Lesion stages

The goal of the initial ablation lesion was to create a lesion that was nontransmural and discontinuous. To achieve this, an intentional gap was created by positioning a 5 mm wide piece of rubber, specifically, a folded water balloon, on both jaws of the ablation clamp, as depicted in Figure 8. RF energy was then applied to the tissue for a single 40-second interval or until the conductance dropped below 2.5 mS, which was intended to produce a nontransmural lesion.

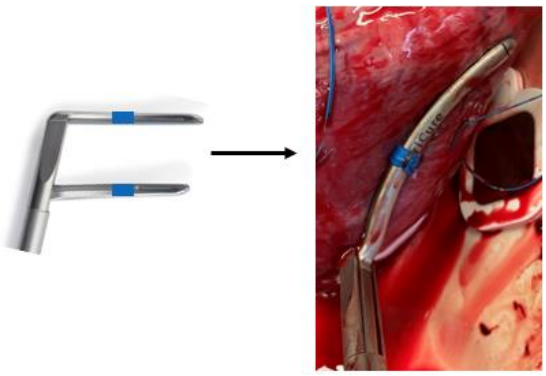

Figure 8 Rubber piece (blue) on the jaws of AtriCure's Isolator Synergy Bipolar clamp.

For the second ablation, the objective was to create a lesion that was (more) transmural, but still discontinuous. The piece of rubber was retained on the ablation clamp, and RF energy was applied for another 40-second interval or until conductance dropped below 2.5 mS.

Finally, for the third and final ablation, the aim was to create a lesion that was both transmural and continuous. The piece of rubber was removed from the clamp, and RF energy was applied until the conductance dropped below 2.5 mS within 5 seconds.

Unipolar high-resolution mapping

Mapping system

During the experiments, epicardial unipolar high-resolution mapping was executed to gather electrophysiological data from the porcine hearts. A 128-electrode array (Figure 9) is used in combination with 120 electrode channels, enabling the simultaneous recording of signals on 120 channels arranged in a 15x8 matrix. The inter-electrode distance is 2 mm and the electrode diameter is 0.65 mm. A bipolar threshold pacing cable is connected to a steel wire around the aortic root, serving as the indifferent grounding electrode. The signals are real-time displayed on a computer monitor, and each measurement is labeled with a corresponding tag to facilitate subsequent analysis. Data were stored on a hard disk after filtering (bandwidth 0-500 Hz), sampling (2 kHz), and analog to digital conversion (16 bits).

Figure 9 128-electrode array used for unipolar high-resolution mappings

Mapping schemes

The epicardial mapping and pacing locations are shown in Figure 10. These locations were measured at baseline and after every ablation lesion, indicating that the full mapping scheme was executed four times.

Every mapping location was measured three times, namely during the intrinsic rhythm, and during pacing from both sides of the lesion. Based on the methods deployed at the EP laboratory to evaluate catheter ablations, it was decided to pace perpendicular to the ablation lesion from two sides during mapping. Pacing perpendicular to the ablation lesion facilitates

the evaluation of conduction through the lesion, and therefore plays a pivotal role in verifying bidirectional conduction block [25, 59].

For pacing, two bipolar pacing wires were stitched to the cardiac tissue at either side of the lesion. This way, the same pacing location throughout different measurements could be guaranteed. A pacing frequency of 100 beats per minute was used, and the pacing threshold was defined by turning the output of the pacemaker up from 1 mA until capture. This way we could avoid the pacing artifact to mask the signal from the heart. The output and pacing rate were noted.

By executing this ablation protocol, the electrophysiological characteristics of the ablation lesions and the intentional conduction gap could be investigated.

The full protocol can be found in Appendix A.

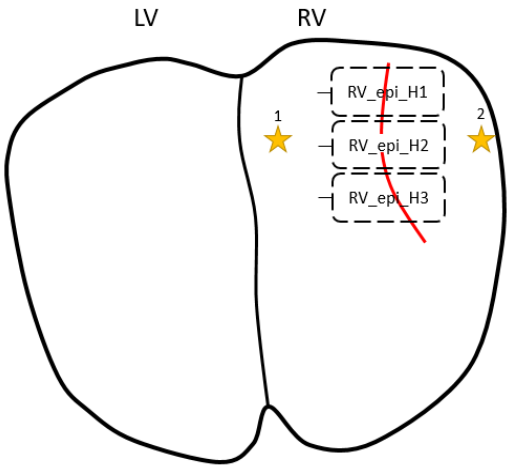

Figure 10 The mapping scheme that is deployed during ex vivo heart perfusion swine experiments. The scheme depicts the locations of the electrode array on the RV for epicardial unipolar high-resolution mapping and the two pacing locations (denoted with a star) perpendicular to the ablation lesion (the red line). *RV = right ventricle; LV = left ventricle; epi = epicardial; H = horizontal*

Data preprocessing

EGMs were analyzed offline using custom-made software developed by the EMC to semi-automatically process the mapping data. The steepest negative slopes (local activation time) of all ventricular potentials were automatically annotated when the amplitude and slope criteria were met.

Amplitude criterion

The amplitude criterion was defined for each electrode separately, based on the voltage noise level on that electrode ($\sigma_{voltage}$), which will be different for each electrode. The noise level determines the level of uncertainty with which the voltages of a sample have been measured. Therefore, the noise level is used to set cut-off values that determine what is to be considered a valid signal and what is not. The amplitude of the candidate deflection should exceed the minimum amplitude ($A_{minimal}$) to be annotated:

$$A_{minimal} > \sqrt{2} \times \sigma_{voltage} \times A_{sigma-detection-level} \qquad Eq.\ 1$$

The $A_{sigma-detection\ level}$ is specified by the user. $\sqrt{2}$ is needed because amplitude is the difference between two voltage samples, such that

$$\sigma_{amplitude} = \sqrt{2} \times \sigma_{voltage} \qquad Eq.\ 2$$

The noise amplitude normalized probability density normal distribution has a total area under the curve of one with a mean of 0 mV and a standard deviation of $\sigma_{amplitude} = 0.05\ mV$, see Figure 11. By setting the $A_{sigma-detection-level}$, the user defines above which level in the normal distribution we consider a measured deflection amplitude to be a valid signal, rather than noise. The probability of a false positive, meaning the deflection is labeled as a valid

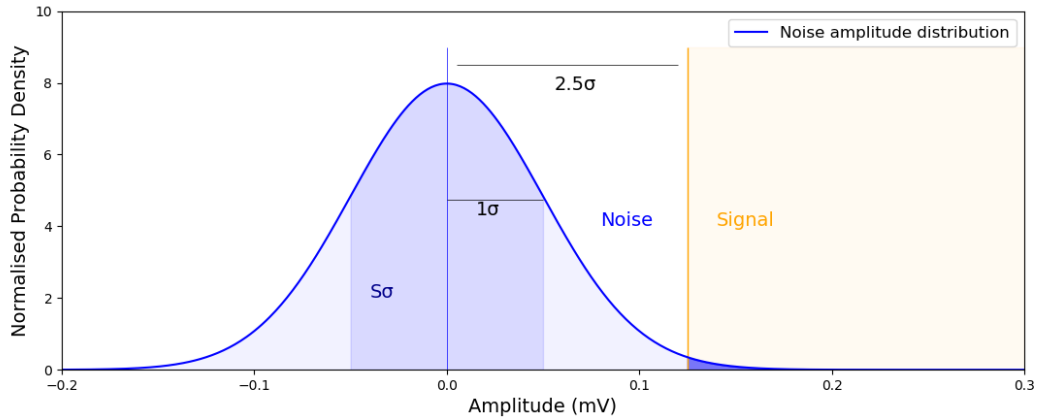

Figure 11 An example of the noise amplitude normalized probability density normal distribution (blue). The user chooses an amplitude level above which she considers a measured potential amplitude to be signal, rather than noise. The probability for a false positive is the probability that the measured potential amplitude belongs to the noise distribution, which is the dark blue shaded area under the blue curve's tail.

deflection while it belongs to the noise distribution, is the dark blue shaded area under the blue curve's tail.

This is what we call P_{error}, the probability that our decision is wrong. Since the total area under the total curve is one, $1 - P_{error}$ gives the area under the tails on both sides of the distribution, and half of this value is the area under one of the tails, see *Eq. 3*:

$$P_{error} = P_{false-positive} = \frac{1}{2} \times (1 - S_{\sigma}) \qquad \textit{Eq. 3}$$

During annotation, the $A_{sigma-detection\ level}$ was set to 2.5, meaning that

$$S_{A-sigma-detection-level} = 0.98758 \text{ or } 98.758\%$$

as follows from the cumulative distribution function of the standard normal distribution.

This gives a P_{error} of

$$P_{error} = \frac{1}{2} \times (1 - 0.98758) = 0.0062 \text{ or } 0.62\%$$

So, only deflections with amplitudes higher than

$$A_{minimal} > \sigma_{amplitude} \times 2.5$$

were considered valid deflections, with a probability for an erroneous decision of 0.62%.

Slope criterion

The absolute slope criterion was manually set to -0.05 V/s. This is the standard setting for atrial annotations. It was chosen to use the same setting for the annotations on the ventricle, to ensure no valid potentials in the ablated area will be missed. So, a potential with a slope of -0.05 V/s or steeper is considered a candidate for valid potentials.

Noise notches

During annotation, the "ignore noise notches" function was used. Sometimes notches occur in a deflection, such that the deflection is divided into two shorter sub-deflections. This "ignore

noise notches" function defines whether a notch is valid or noise, and in case of noise, the notch is ignored and considered part of the deflection. A notch is considered noise when the minimum of the first and the maximum of the second sub-deflection are less than or equal to 3 ms apart, and if the amplitude is lower than the amplitude criterion.

Annotation process continued

All annotations were visually verified and manually adjusted when needed with consensus of two investigators. Areas of simultaneous activation were excluded from the analysis to avoid the inclusion of far-field potentials. Electrically silent electrodes were either not annotated by Annotation Tool in the first place, or the annotations were manually deleted in case of only noise, far-field, or baseline drift. Electrical silence means the absence of measurable activity in the cardiac tissue.

Data analysis

All further data analysis was executed using dedicated software developed in Python. In Python, electrodes without annotations could either be broken electrodes or electrically silent electrodes. To distinguish between these, broken electrodes were labeled with a value of -20. The label of electrically silent electrodes varied depending on the parameter analyzed.

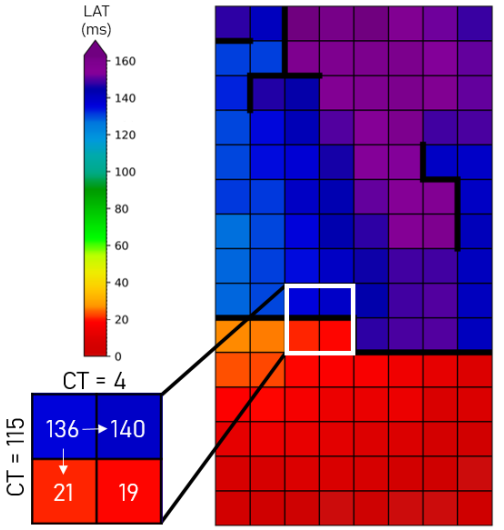

Figure 12 Color-coded activation map and an example of inter-electrode conduction time calculation by subtracting the local activation time of each electrode from the adjacent right and lower electrode. Black lines indicate block lines (inter-electrode conduction time > 12 ms).

Activation maps

Color-coded activation maps were reconstructed as shown in Figure 12. The presence of a conducting gap was verified by activation mapping (i.e., conduction through the ablation gap). Local activation times of electrically silent electrodes were labeled with "not a number" and therefore result in white squares in the activation maps. Conduction block is indicated by a black line (see section "Conduction times").

Conduction times

Inter-electrode conduction times (CT) were calculated by subtracting the local activation time of each electrode from the adjacent right and lower electrodes (Figure 12). This results in an array with "vertical" CTs, and "horizontal" CTs. In instances where an electrode was electrically silent, the CT was calculated by subtracting the local activation time of the subsequent electrode that exhibited signals. This was not performed for malfunctioning electrodes, since this might result in false positive prolonged CTs.

The change in CT over the different stages of ablation on the electrodes surrounding the lesion was analyzed. CTs bigger than 12 ms, corresponding with a conduction velocity of < 17 cm/s, have been defined as a line of conduction block in previous research [60].

EGM morphology

The morphology of EGMs was characterized by the voltage, slope, and R-to-S-amplitude ratio (R/S ratio) of the potentials. Unipolar voltage was analyzed as the peak-to-peak amplitude of potentials. The potential slope was calculated by differentiating the potential voltage with respect to time, see Figure 13. Potentials with a duration exceeding 50 ms were omitted from voltage and slope analysis as they are likely to have merged into a far-field signal or baseline drift, as such prolonged durations are uncommon. The potential voltage and slope of electrically silent electrodes were converted to 0 mV or 0 V/s, respectively.

Unipolar single potentials are characterized by a rapid negative deflection preceded by a positive R-wave and returning to the baseline (S-wave) [61], see Figure 14. The R/S ratio of a single potential is calculated by dividing the amplitude of the R-wave by the amplitude of the S-wave. Before doing so, the signal was corrected for baseline drift. The potential of interest, which encompasses a window of 30 ms prior and 60 ms after the primary local activation time, is extracted from the signal on that electrode. A low-pass filter is applied to the remaining signal, allowing frequencies below 15 Hz to pass. This way, only the low frequencies remain, which is deemed baseline drift. The excised portion is filled by interpolation. Then, the baseline drift is subtracted from the potential of interest, resulting in a potential corrected for the baseline drift.

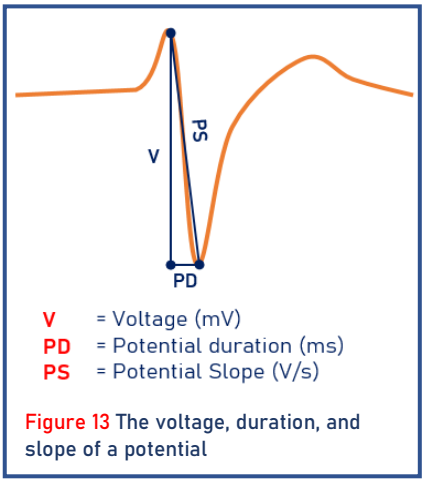

Figure 13 The voltage, duration, and slope of a potential

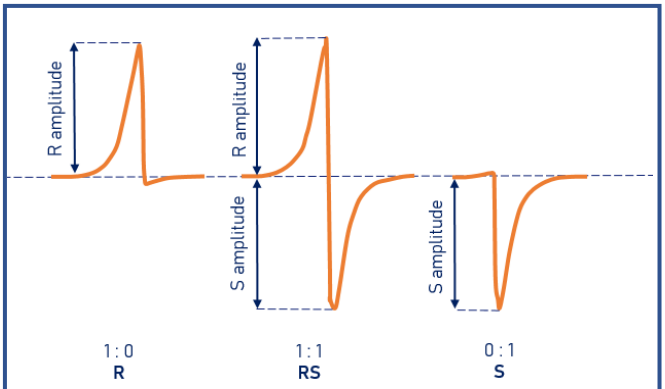

Figure 14 Potentials with variable R/S ratios, calculated by dividing the R-wave amplitude by the S-wave amplitude

Single potentials and primary potentials of some long DPs in the EGMs were classified according to their relative R- and S-wave amplitude and scaled from -1 (R-wave) to 1 (S-wave):

$$RS = \begin{cases} 1 - RS(n) & \text{for } RS(n) \leq 1 \\ \dfrac{1}{RS(n)} - 1 & \text{for } RS(n) > 1 \end{cases} \qquad Eq.\ 4$$

The R/S ratio of electrically silent electrodes was set to -40, which is an impossible value for the R/S ratio, and could therefore easily be selected to be excluded from analyses. R/S ratios were calculated only for single potentials and some long DP. Long DPs could only be considered if the secondary potential was not located at the point where the potential of interest (primary potential) is cut off (30 ms before and 60 ms after the local activation time). This was to ensure the accuracy of the interpolation process. If a noise notch divided a deflection into two sub-deflections, it was treated as a single deflection in the R/S ratio calculation, provided that the sub-deflection before or after the notch exceeded a specified threshold (0.5 mV and the noise level). The same time and amplitude criteria as used during annotation were used to detect a

noise notch for the R/S ratio calculation. R/S ratios of all short DPs and fractionated potentials were excluded from analysis and assigned a value of "not a number" due to the current lack of a proper method for defining R/S ratios in these types of potentials.

Definition of ablation lesion area

The location of the ablation lesion was defined based on the location of the highest vertical median (per electrode) CT per column and the presence of electrically silent electrodes. If there are no electrically silent electrodes, as in Figure 15, the electrodes directly next to the block line (continuous black line) are noted as the electrodes next to/on the ablation lesion. In this case, the blue/purple electrodes are noted as the electrodes distal of the lesion, and the red/orange as proximal of the lesion. If there was an even amount of electrically silent electrodes in a column of the electrode array, half was considered proximal to the lesion and the other half distal to the lesion. If it was odd, the larger portion was allocated to the distal site. Per mapping file, the ablation lesion and a small area around it were analyzed in detail. This "lesion area" was defined as four electrodes distal and four proximal to the ablation lesion per column, resulting in 32 electrodes proximal to the lesion and 32 distal. This means an area of 16 mm (8 electrodes multiplied by the inter-electrode distance of 2 mm) around the center of the ablation lesion was analyzed in detail to detect changes in EGM morphology caused by ablation. The cut-off of 16 mm was based on previous research which showed that ablation caused effects in the tissue in an area of 14 mm around the center of the lesion [62].

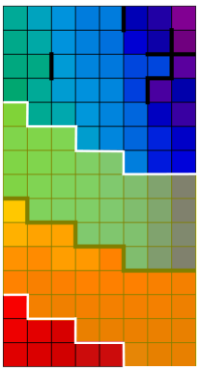

Figure 15 The yellow highlighted area within the white lines is the area around the lesion that was studied and compared in detail across different ablation lesions.

Lesion distance dependent changes in electrophysiological parameters

The potential voltage, potential slope, and R/S ratio were assessed as a function of distance from the ablation lesion. This examination aimed to determine if the parameters change gradually or abruptly and to understand the nature of these changes.

Statistical analysis

For every electrode in every mapping file, the median of the analyzed parameter was calculated over the different wavefronts. The median was used due to a small sample size – every file contained between 6 to 12 waves. This results in 120 medians per mapping file (assuming there are no broken electrodes). Histograms were made to show the relative frequency distribution of parameters over all porcine hearts and ablation lesions. The relative frequency was expressed as a percentage of the total amount of electrodes (amount of patients times 120).

The median and interquartile range (IQR) for the parameters of interest were calculated across the area of 16 mm (64 electrodes) around the center of the ablation lesion to analyze the change in the EGM morphology near the ablation lesion. The median and IQR for the vertical CT across the ablation lesion were also calculated. Wilcoxon Signed Rank Tests were used to compare the medians between the three stages of ablation lesions. The Wilcoxon Rank Sum Test was used to verify differences between the continuous and discontinuous lesion parts within the same lesion. A p-value of less than 0.05 was considered statistically significant.

Results

Ex vivo perfused porcine hearts

Of the eight EVHP experiments with DCD porcine hearts, three were included. In one of the included hearts, mapping locations H1 and H3 were incomplete and were thus excluded from analyses. Five experiments were excluded for various reasons. The first experiment was performed on an antelope heart rather than porcine and was primarily a trial experiment. In the fourth and fifth experiments, pacing location 2 was inadvertently switched to biventricular pacing. The seventh and eighth experiments were performed too late in the course of this master's thesis to be considered. So, a total of 68 mapping files were included. An overview of the included experiments is given in Table 1. A detailed record of all experiments can be found in Appendix C.

Table 1 Details on included experiments

Subject	Measured	Mapping complete?	Intrinsic rhythm	Pacing rate [bpm]	Pacing output [mA]	Warm ischemic time	Total ischemic time
N2	RV	No*	No	100	5	3:58	1:56:19
N3	RV + LA	Yes	No	100	5	4:00	1:55:28
N6	RV + LA	Yes	Yes	100	2	3:58	1:56:15

* Measurements of H1p1, H1p2, H3p1 and H3p2 of the baseline measurement and lesion 1 are missing.

Transverse sections

Figure 16 shows an example of transverse sections of the heart that were made at the end of every experiment. A portion of the ablation lesion is shown in a close-up. Visually, this is a transmural ablation. Note that all three ablation lesions were subsequently created at the same location on the RV, so this visual analysis could be performed only for the third lesion. The lesion width of the third lesion was measured in some of the experiments and did not exceed 5 mm.

Activation maps

The electrical activation patterns of the hearts with and without ablation lesions were visualized by activation maps. Figure 17 shows examples of color-coded activation maps with isochrones (black lines) drawn at 10 ms intervals. The black arrows indicate the main wavefront direction. Straight black lines between electrodes indicate CTs greater than 12 ms, which is generally considered a conduction block [63]. The white squares indicate electrically silent electrodes, and in the data gathered for these experiments that also means conduction block.

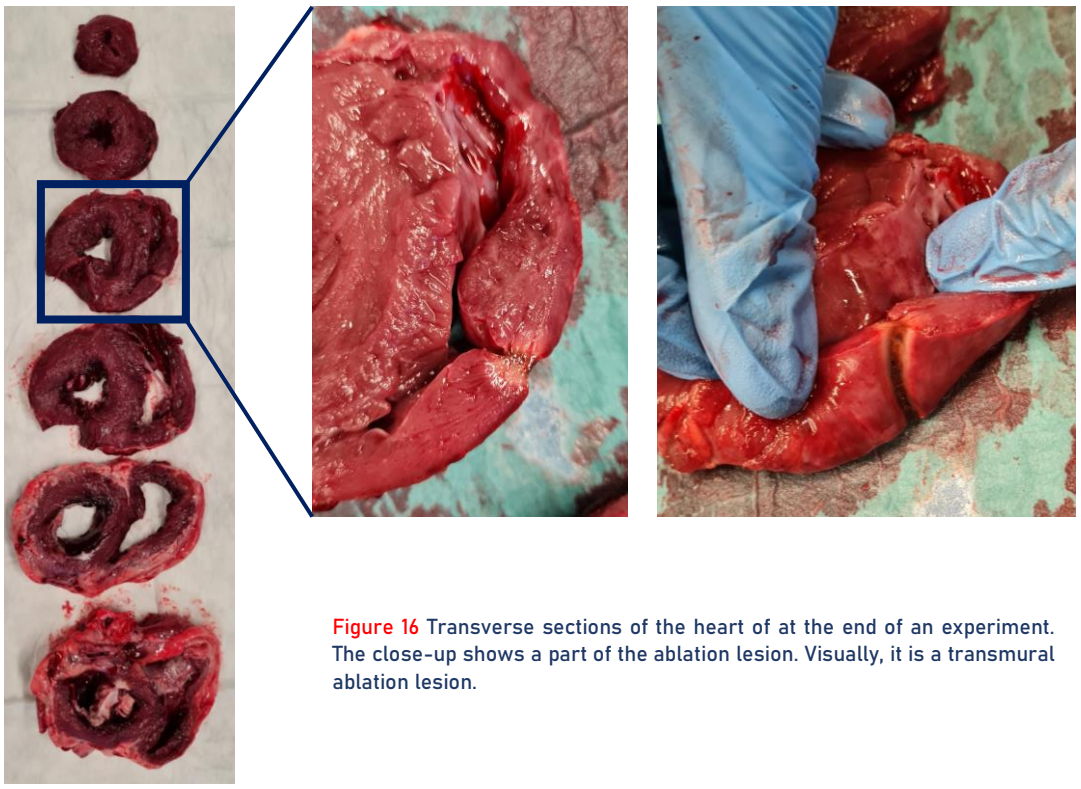

Figure 16 Transverse sections of the heart of at the end of an experiment. The close-up shows a part of the ablation lesion. Visually, it is a transmural ablation lesion.

The example EGMs were measured in subject N2 on location H2 during pacing from location 1. The orientation of the electrode array and the pacing location is shown in the baseline image. The baseline activation map, derived before ablation, shows a smooth wavefront propagation over the cardiac tissue. The wavefront enters the electrode array on the lower right corner and propagates to the upper left corner, only encountering some negligible small block lines located diffusely, without significantly affecting the wave propagation. In one of three swine (33.3%), a focal conduction gap was detected on the activation map in the first ablation lesion generated, whereas in the remaining two swine (66.6%) no conduction gap was visible in the activation maps. This is shown in the activation map of lesion 1. The ablation lesion is located approximately in the center under the electrode array, indicated by the block line that spans the entire width of the electrode array. Like in the baseline measurement, the wavefront enters from the lower right corner, indicating that the position of the electrode array on the heart is similar. However, now the wavefront encounters a line of block caused by ablation. Interestingly, the wavefront reappears from the center of the ablation lesion on the opposite side and spreads from there in two directions. This results in a total of three wavefronts in the activation map. In the activation maps of lesion 2 and 3, the wavefront travels around the ablation lesion and comes back in from the side(s) of the electrode array on the other side of the ablation lesion. In all other subjects, this effect occurs immediately after the first ablation lesion. Also, in one subject, ablation resulted in more electrically silent electrodes compared to the other two subjects. Outside of these exceptions, this example is representative of the other activation maps.

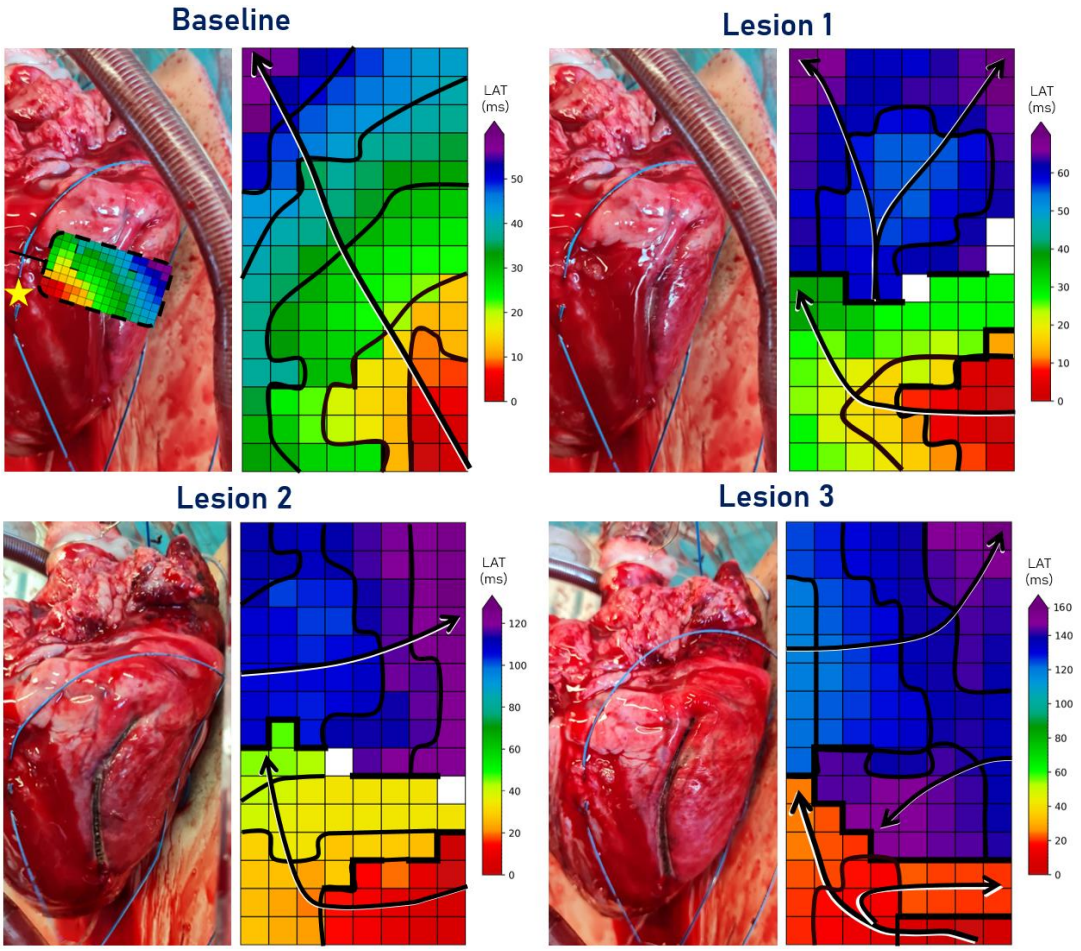

Figure 17 Examples of color-coded activation maps with isochrones (black curvy lines) drawn at 10 ms. The black arrows indicate the main wavefront directions. The white squares indicate electrically silent electrodes. Straight black lines inbetween electrodes indicate conduction times bigger than 12 ms, which is generally regarded as conduction block. These EGMs are measured in subject N2 on location H2 during pacing from location 1. The orientation of the electrode array and the pacing location are shown in the baseline picture. The ablation lesion is located approximately halfway under the electrode array. In the EGMs of lesion 1, 2, and 3, a line of block that stretches over the whole width of the array is visible. This is indicated by the block lines and/or electrically silent electrodes, and by the jump in local activation time as indicated by the color.

Conduction times

For each mapping file, the median and IQR were determined for the vertical CTs across the ablation lesion. A maximum of eight CTs per file were considered, corresponding to the width of the electrode array, since the ablation lesion is located perpendicular to the array. Subsequently, the medians and IQRs of mapping locations H1 and H3, without an intentional conduction gap (n = 10), and mapping location H2, with an intentional conduction gap in lesion 1 and 2 (n = 7) were calculated, see Figure 18.

A significant steep increase in CT is seen between baseline and lesion 1 for all mapping locations. The Wilcoxon Signed Rank Test showed no significant differences in median CT between the different lesions for all mapping locations. Also, the Wilcoxon Rank Sum Test showed no significant differences between the locations with (H2) and without (H1/H3) an intentional gap. However, a continuous and gradual increase in the median CT is observed at

Figure 18 Conduction times (ms) for each ablation lesion for mapping locations H1 and H3 (without any conduction gaps) and mapping location H2 (with intentional conduction gap). The bar graphs show the median and interquartile range (IQR) of the vertical conduction times across the ablation lesion for baseline and three stages of ablation lesions. A steep and significant rise in conduction time is seen after the first ablation lesion compared to baseline for all locations. The Wilcoxon Signed Rank Tests shows no significant differences in conduction time between the different lesions. The Wilcoxon Rank Sum Test showed no significant differences between the conduction times between H2 and H1/H3.

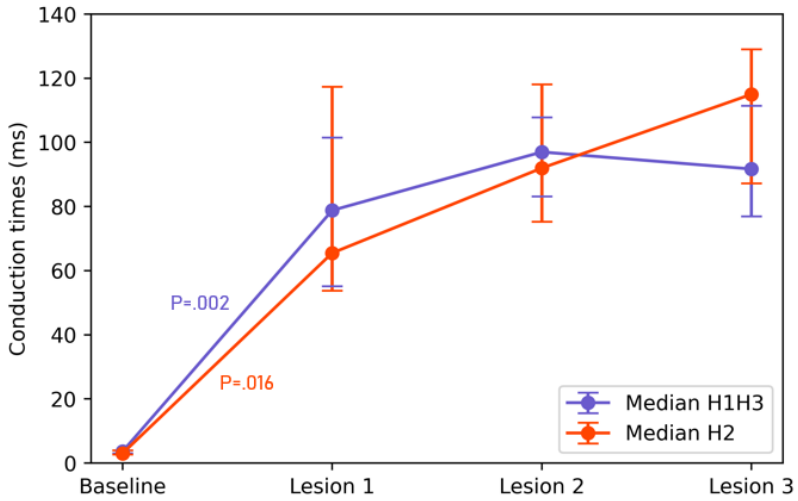

N	10	10	10	10
Median	3.6	78.8	97.0	91.7
IQR	3.1-4.0	55.2-101.5	83.2-107.8	77.0-111.4

N	7	7	7	7
Median	3.0	65.5	92.0	115.0
IQR	2.7-4.0	53.8-117.4	75.3-118.1	87.2-129.1

mapping location H2, compared to mapping locations H1 and H3, where the increase in CT was steeper between baseline and lesion 1, but remained more stable across the three lesions.

Figure 19 highlights two example files for mapping location H2 that may partially explain this difference. The left panel shows the CTs of the swine with a conduction gap detected on the activation map in the first ablation lesion. It is noticeable, that the increase in CT from baseline to lesion 1 is smaller compared with the other subjects and that the increase in CT continues in subsequent lesions 2 and 3. The right panel in Figure 19 shows a more representative example of the other files, in which a steep increase in CT is seen between baseline and lesion 1, followed by a more stable CT. Another discrepancy in the data is that the increase in CT between baseline and lesion 1 is the smallest in the files measured during intrinsic rhythm for mapping location H1 and H3. Measurement during intrinsic rhythm at mapping location H2 also showed a smaller increase compared with pacing, except for the swine with the conduction gap on the activation map, which showed even a smaller increase in CT between baseline and lesion 1. Inter-individual differences exist, for which the tables with all separate values for median and IQR are listed in Appendix D.

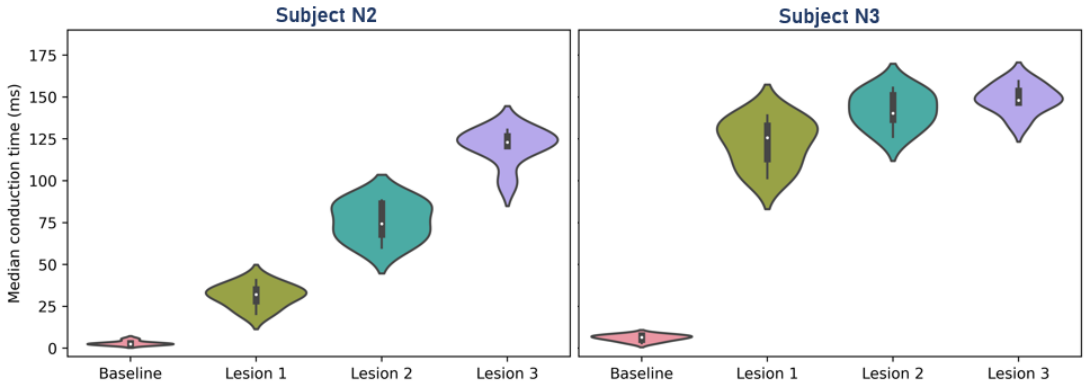

Figure 19 The median conduction times (over the different waves) across the ablation lesion for two files of two subjects, as an example. The left panel shows mapping location H2p1 of subject N2, the only subject in which the conduction gap was visible in the activation map of lesion 1. The right panel shows H2p1 of subject N3, which is more representative for the other files.

Electrogram morphology

Figure 20 shows two representative variations of how ventricular potentials change nearby and at a distance from the ablation lesion. This shows in one figure how the voltage, slope, R/S ratio, and CT of the potentials can change in the direction of the lesion.

The left example in Figure 20 is an activation map on location H1 from subject N3 after the first ablation lesion while pacing from location 1. The change of potentials towards the ablation lesion in the fifth column of the electrode array is visualized. The electrode on/next to the ablation lesion shows a DP, which is a sign of conduction block [25]. It shows the time delay during which the wavefront travels around (or across) the ablation lesion. The values of potential voltage, potential slope, and R/S ratio on the electrodes surrounding the lesion are listed in the figure for reference. The voltage of the DP suddenly dropped by 50-70% compared to the potentials surrounding the DP. The potential slope drops by 50-75%. Despite the sudden sharp drop, the value of the voltage is still quite significant. The R/S ratio in the ablation lesion area is quite constant in this example. From the DP, only the R/S ratio of the primary deflection can be calculated. The R-wave is more prominent in the DP compared to the surrounding electrodes. Also, the DP is very distinct on one of the electrodes, and in the directly adjacent electrodes, one of the potentials completely disappeared. In some of the files, the DP extended over several neighboring electrodes instead of suddenly disappearing.

The right example in Figure 20 is from subject N6, mapping location H2 while pacing from location 2, after ablation lesion 2. Two electrodes in this column became electrically silent. A gradual decrease in potential voltage and slope is observed at shorter distances from the lesion. The voltage and slope of the potential above the electrically silent electrodes could not be calculated due to baseline drift and/or far-field signal that merged with the potential, resulting in a long duration of the signal and unreliable values for voltage and slope. In the R/S ratio, a shift takes place from equal R- and S-amplitude contributions to an R-wave that becomes more prominent closer to the lesion and eventually becomes almost a monophasic R wave. This gradual change is not seen during all tests. In some examples, a sudden change from high voltage, steep potential slope, and equal R- and S-wave contributions, to electrically silent is seen.

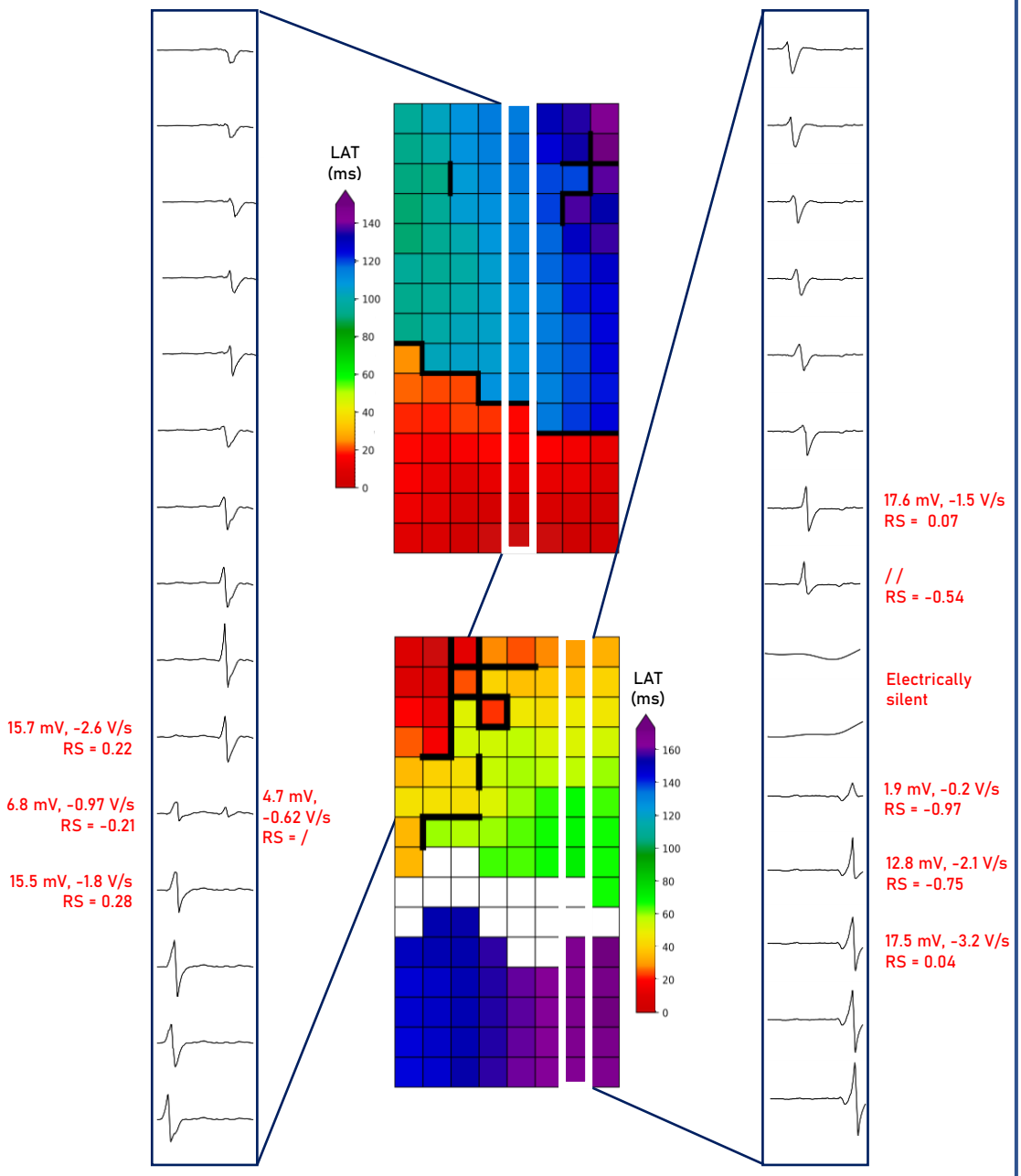

Figure 20 Examples of two color-coded activation maps. In each of them, the potentials of one column in the electrode array are highlighted and visualized. The potentials have been corrected for baseline drift. This shows two variations of how EGM properties can change as a function of distance from the ablation lesion. In the top/left example (subject N3, lesion 1, H1p1) the black line indicates the position of the ablation lesion. In the lower/right example (N6, lesion 2, H2p2) this is indicated by the white squares (electrically silent electrodes). The potential voltage, slope, and R/S ratio values of the electrodes surrounding the lesion are listed for reference. The R/S ratio was not calculated for secondary deflections. On the right side, the voltage and slope of one potential were not listed, because this potential merged with baseline drift/far-field signal before baseline correction was applied and was therefore excluded from voltage and slope calculations.

Voltage

Figure 21 shows histograms of mapping locations 1, 2, and 3 during pacing from location 1. The y-axis shows the relative frequency distribution of the median potential voltage (per electrode, calculated over the different waves) at each mapping location across the different stages of the ablation lesion.

In all three baseline measurements, the potential voltage range between 0 and 12 mV is very little expressed. Most voltages fall in the range between 12 and 27 mV. After the first ablation lesion, the range between 0 and 12 mV becomes more pronounced, and the voltages above 12 mV less, resulting in a shift towards the left in the frequency distribution. This trend was consistent across the subsequent two ablation lesions, meaning the lower region, especially between 0-3 mV, becomes even more expressed. Note that the voltage of electrically silent electrodes was turned into 0 mV. The histograms while pacing from location 2 or during the intrinsic rhythm (only measured in subject N6) showed similar trends and can be found in Appendix D.

The area around the lesion, defined as a diameter of 16 mm around the ablation lesion (8 mm on both sides, see Method section "Definition of ablation lesion area"), was examined in detail. The medians and IQRs of voltage in the lesion area are shown in Figure 22. Wilcoxon Signed Rank Tests revealed that the voltage decreases significantly between baseline and lesion 1 and between all different stages of ablation lesions, for both mapping location H2 (intentional conduction gap in lesion 1 and 2) and H1/H3 (no intentional conduction gap). The tables provided in Appendix D can be reviewed for inter-individual differences.

When comparing tests with and without an intentional gap in lesions 1 and 2, the decrease in median voltage in H2 is smaller from baseline to lesion 1 compared to H1/H3, resulting in a significantly higher voltage for the gap location, as shown by the Wilcoxon Rank Sum Test. Subsequently, the median voltage in lesion 2 becomes comparable for all mapping files, indicating a bigger decrease in voltage is seen for mapping location H2 between lesion 1 and 2. The decrease in voltage between lesion 2 and 3 is comparable for all mapping locations.

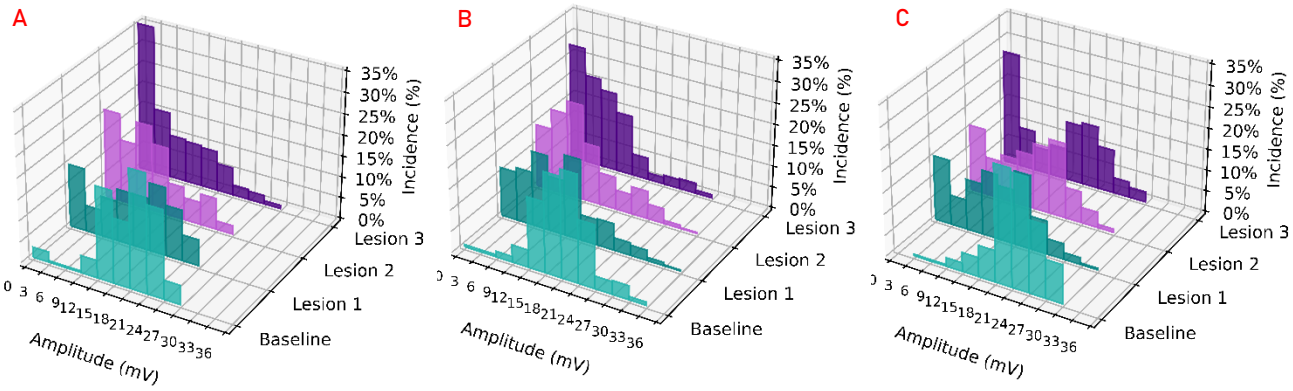

Figure 21 Histograms of the relative frequency distribution of median voltages (per electrode over the different waves) over the different lesion stages. These voltages were recorded during pacing from location 1, in mapping locations A) H1; B) H2; C) H3. Subjects N3, and N6 are combined in the histograms of location H1 (A) and H3 (C). N2 was not included because only lesion 2 and 3 were measured for these mapping locations. Subjects N2, N3, and N6 are combined in the histogram of location H2 (B).

Figure 22 Voltages per ablation lesion for mapping locations H1 and H3 (without any intentional conduction gaps) and H2 (with intentional conduction gap). The bar graphs show the median and interquartile range (IQR) of potential voltage for baseline and three stages of ablation lesions. The Wilcoxon Signed Rank Tests show that the voltage declines significantly with every subsequent ablation for all mapping locations. The Wilcoxon Rank Sum Test showed that the voltage in the continuous lesion parts differs significantly from the discontinuous parts in lesion one (denoted by the black star).

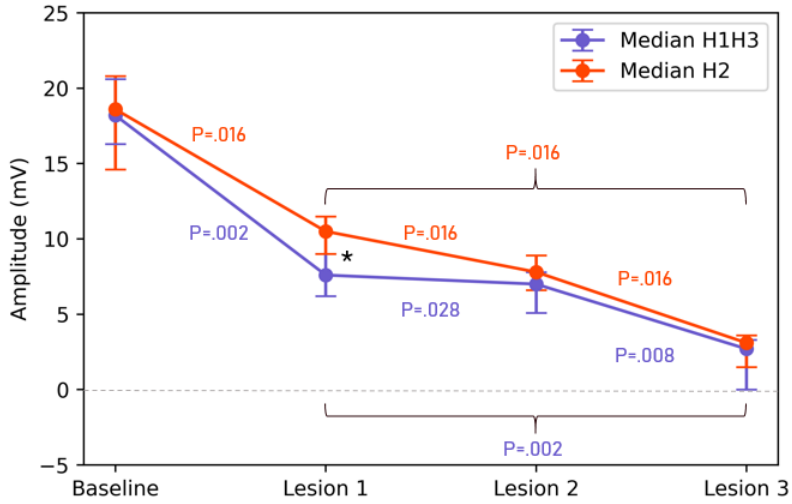

N	10	10	10	10
Median	18.2	7.6	7.0	2.7
IQR	16.3-20.6	6.2-9.0	5.1-7.8	0.0-3.3

N	7	7	7	7
Median	18.6	10.5	7.8	3.1
IQR	14.6-20.8	9.0-11.5	6.6-8.9	1.5-3.6

Figure 23 illustrates a specific example of subject N6, mapping location H1, to illustrate the voltage trend in more detail. The median voltage change in relation to the distance from the ablation lesion across different lesion stages is visualized. The subplots on the left represent the proximal side of the ablation lesion, while the subplots on the right represent the distal side. The x-axis depicts the distance from the lesion, measured in electrodes (inter-electrode distance of 2 mm), and on how many values the boxplots are based. Because the lesion is not always perfectly aligned in the center of the electrode array during measurement, the number of electrodes on the proximal and distal sides of the ablation lesion may be different. Also, values can be missing due to malfunctioning electrodes or potentials with a duration longer than 50 ms. For the baseline measurement, the location of lesion 1 was used to divide the array into two subplots. Baseline voltage differs somewhat between measuring during pacing from locations 1 and 2, and during intrinsic rhythm. In addition, voltages during baseline are slightly higher on average on the proximal side of the electrode than on the distal side. After the first ablation lesion, the overall voltage decreases at all distances from the lesion. The decline is more pronounced closer to the lesion, resulting in a gradual change in voltage toward the lesion. After ablation lesions 2 and 3, the voltages distant from the lesion remain stable compared to the previous lesion, but the area of low voltages or electrically silent electrodes expands to a larger area in proximity of the lesion. Of the subjects, N6 had the most electrically silent electrodes in all measurements, but the trends of voltage change observed in the other hearts were similar. These graphs also show that the voltage change with and without pacing is comparable.

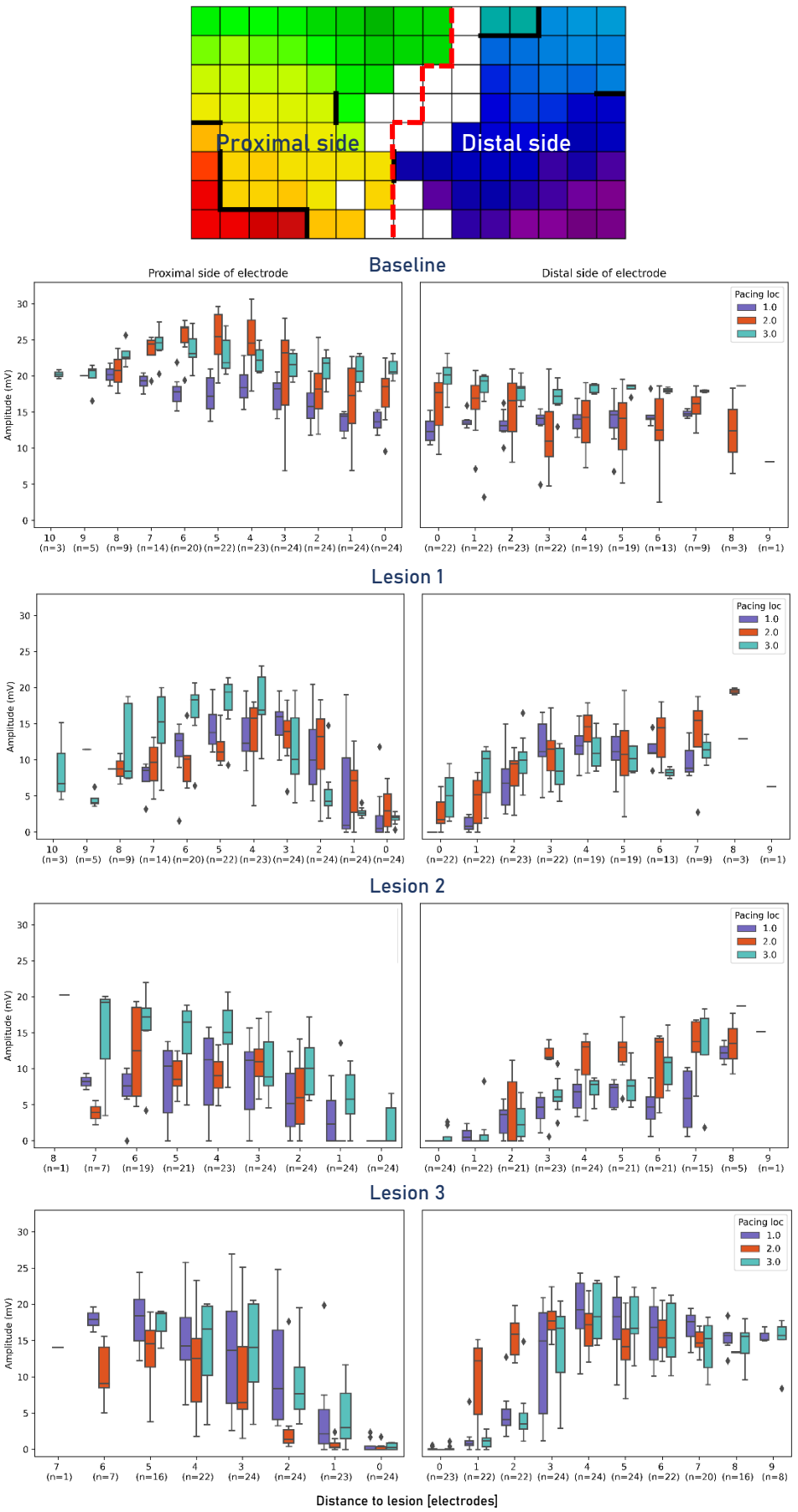

Figure 23 The change of the potential voltage (mV) (y-axis) in relation to the distance from the ablation lesion measured in electrodes (x-axis). The inter-electrode distance is 2 mm. It is noted on how many values the boxplot is based under the x-axis. The maximum value of n is 24. Missing values can be due to malfunctioning electrodes or potentials with a duration longer than 50 ms. Voltages of mapping location H1 in subject N6 are shown. An example activation plot of the first lesion while pacing from location 1 is shown at the top to visualize the alignment of the electrode array with the plot. The left subplots show the site proximal of the ablation lesion (left of red dotted line in activation map) and the right subplots the distal side (right of dotted line in activation map).

Potential slope

Figure 24 shows histograms of potential slopes for the same mapping locations shown for voltage. From baseline to lesion 3, there is a gradual shift of the frequency distribution to the right, implying that the potential slopes become less steep as more ablation is applied. It should be noted that potential slopes in the lower range (0-1 V/s) are already present in the baseline measurements. The potential slopes of electrically silent electrodes were analyzed as 0 V/s. The histograms during pacing from location 2 show similar trends. The potentials measured during intrinsic cardiac rhythm at locations 2 and 3 show steeper slopes during baseline and all subsequent lesions compared with the histograms shown, but the trend for the slopes to become less steep with ablation is still evident. A complete overview of the slope histograms can be found in Appendix D.

To analyze the effects of the stage of ablation ((non)transmurality and (dis)continuity) on the potential slope, we zoom in on the lesion area. Figure 25 displays the medians and IQRs of the potential slopes in the lesion area. The steepness of the slope decreases from baseline to lesion 1. Subsequently, the Wilcoxon Signed Rank Test revealed no significant difference between lesion 1 and 2 for all mapping locations, whereas a significant decrease in steepness is seen between lesion 1 and 3 and lesion 2 and 3 for all mapping locations. The medians and IQRs of all tests can be found in Appendix D. The Wilcoxon Rank Sum Test showed no significant differences between the locations with (H2) and without (H1/H3) an intentional gap, as the trends are very similar.

Figure 26 shows the trend for the potential slope in detail. The change in median potential slope as a function of distance from the ablation lesion for subject N6, mapping location H1 is visualized (same example as given for voltage). Potential voltage and slope follow similar trends. The lower the voltage, the less steep the slope, although slopes have larger IQRs than the voltage for most electrodes. However, near the ablation lesion, the IQRs become smaller. Also, the area with small IQRs around the ablation lesion widens with subsequent lesions and shows less steep potential slopes. Most of the files from the other subjects follow the same trend. The other subjects show less electrically silent electrodes, but very narrow IQRs with a value close to 0 V/s near the lesion. For some of the subjects, the potential slopes are already quite low at baseline, but the same trend of a decreasing slope can be seen.

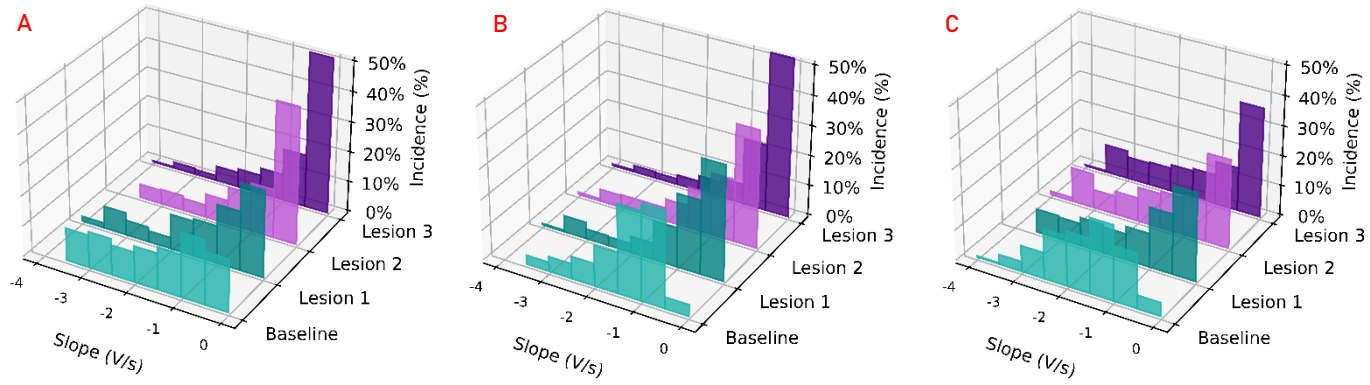

Figure 24 Histograms of the relative frequency distribution of potential slopes (V/s) over the different lesion stages during pacing from location 1, in mapping locations A) H1; B) H2; C) H3. Subjects N3, and N6 are combined in the histograms of location H1 (A) and H3 (C). Subjects N2, N3, and N6 are combined in the histogram of location H2 (B).

Figure 25 Potential slope (V/s) per ablation lesion for mapping location H1 and H3 (without any intentional conduction gaps) and H2 (with intentional gap). The bar graphs show the median and interquartile range (IQR) of the potential slopes for baseline and three stages of ablation lesions. The Wilcoxon Signed Rank Tests show that the slopes between lesion 1 and 2 do not change significantly for all mapping locations, but becomes significantly less steep between baseline and lesion 1, lesion 2 and 3 and lesion 1 and 3 for all mapping locations. The Wilcoxon Rank Sum Test showed no significant differences between the potential slopes between H2 and H1/H3.

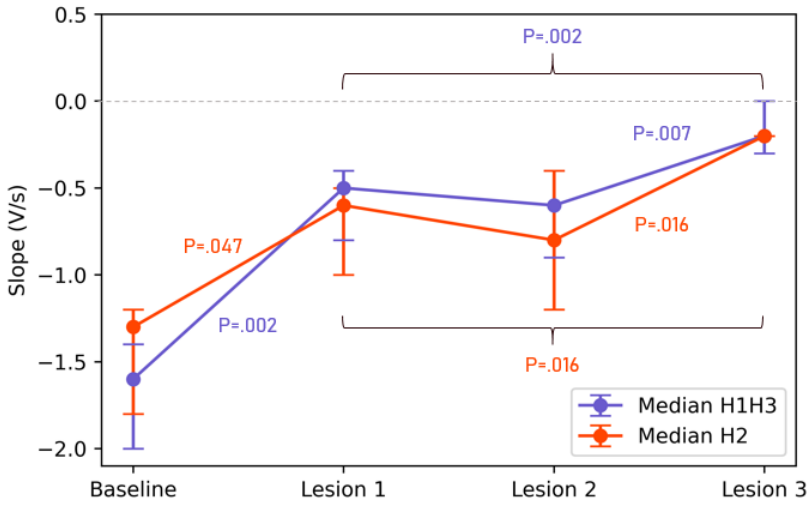

N	10	10	10	10
Median	-1.6	-0.5	-0.6	-0.2
IQR	-2.0--1.4	-0.8--0.4	-0.9--0.4	-0.3-0.0

N	7	7	7	7
Median	-1.3	-0.6	-0.8	-0.2
IQR	-1.8--1.2	-1.0--0.5	-1.2--0.4	-0.2--0.2

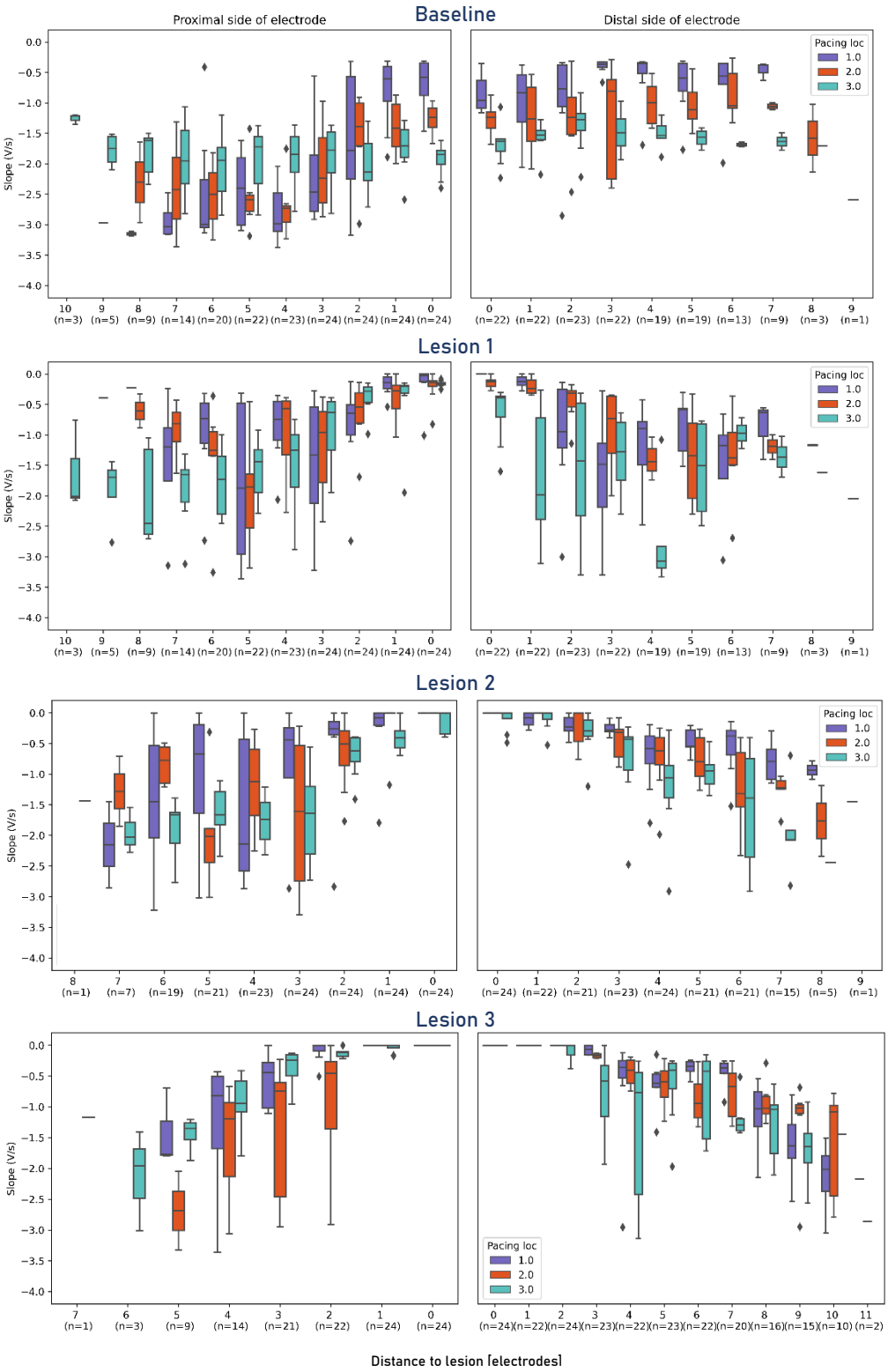

Figure 26 The change of the potential slope (V/s) (y-axis) in relation to the distance from the ablation lesion measured in electrodes (x-axis). The inter-electrode distance is 2 mm. It is noted on how many values the boxplot is based under the x-axis. The maximum value of n is 24. Missing values can be due to malfunctioning electrodes or potentials with a duration longer than 50 ms. The potential slopes of mapping location H1 in subject N6 are shown. The left subplots show the site proximal of the ablation lesion and the right subplots the distal side.

R/S ratio

R/S ratios are ranked from -1 (R-waves) to 1 (S-waves). An R/S ratio of 0 means an equal contribution of the R- and S-wave. Figure 27 depicts the R/S ratios in the lesion area. At baseline, the S-wave is more pronounced than the R-wave. After the first ablation lesion, the contribution of the R-wave increases compared with baseline, but the S-wave is still more prominent than the R-wave. From lesion 1 to 3, the R-wave becomes more prominent overall and reaches a median of 0.0 and -0.1 for H1/H3 and H2, respectively, at the third lesion. Also, the IQR includes negative values, indicating that for some signals, the R-wave becomes more prominent than the S-wave. When evaluating the medians and IQRs of all the files separately (see Appendix D), some IQRs even include -1, indicating monophasic R waves.

Wilcoxon Signed Rank Tests show that the contribution of the R-wave becomes significantly greater between baseline and lesion 1, between lesion 2 and 3, and between lesion 1 and 3 for both mapping locations H1/H3 (without intentional conduction gap) and mapping location H2 (intentional conduction gap in lesion 1 and 2). There is no significant difference in the R/S ratio between lesion 1 and 2. The Wilcoxon Rank Sum Test showed no significant differences between the locations with (H2) and without (H1/H3) an intentional gap.

The influence of ablation on the median R/S ratio is depicted in more detail in the example of subject N6 at mapping location H3 in Figure 28. The figure shows the alteration in R/S ratio as a function of the distance from the ablation lesion, both during pacing and intrinsic rhythm. Both during pacing and during intrinsic rhythm, the R-wave becomes more prominent with shorter distance from the ablation lesion. It is worth mentioning that the boxplots closest to the lesion are often based on a limited number of values, due to the presence of electrically silent electrodes, broken electrodes or short DPs, fractionated potentials, or long DPs that do not meet the annotation criteria (see Method section "EGM morphology").

Figure 27 R/S ratios per ablation lesion for mapping location H1 and H3 (without any intentional conduction gaps) and H2 (with intentional gap). The bar graphs show the median and interquartile range (IQR) of the R/S ratio for baseline and three stages of ablation lesions. The Wilcoxon Signed Rank Tests show that the contribution of the R-wave becomes significantly more prominent between baseline and lesion 1, between lesion 2 and 3 and between lesion 1 and 3 for all mapping locations. The Wilcoxon Rank Sum Test showed no significant differences between the R/S ratios between H2 and H1/H3.

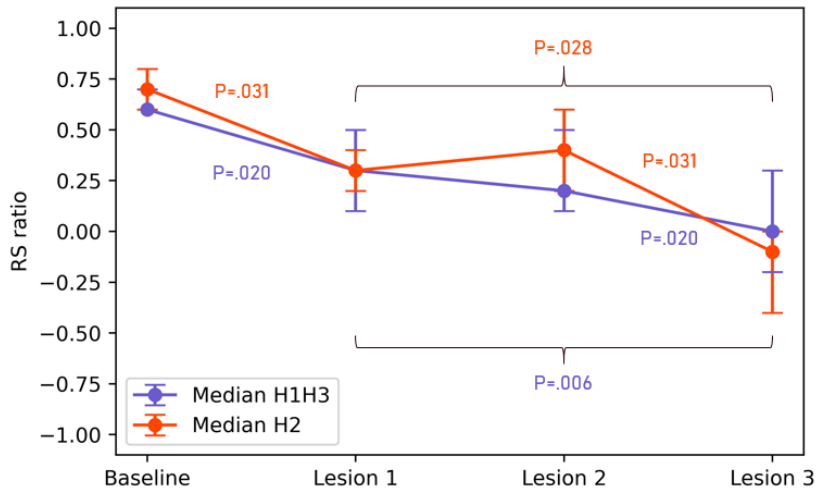

	Baseline	Lesion 1	Lesion 2	Lesion 3
N	10	10	10	10
Median	0.6	0.3	0.2	0.0
IQR	0.6-0.7	0.1-0.5	0.1-0.5	-0.2-0.3

	Baseline	Lesion 1	Lesion 2	Lesion 3
N	7	7	7	7
Median	0.7	0.3	0.4	-0.1
IQR	0.6-0.8	0.2-0.4	0.2-0.6	-0.4-0.0

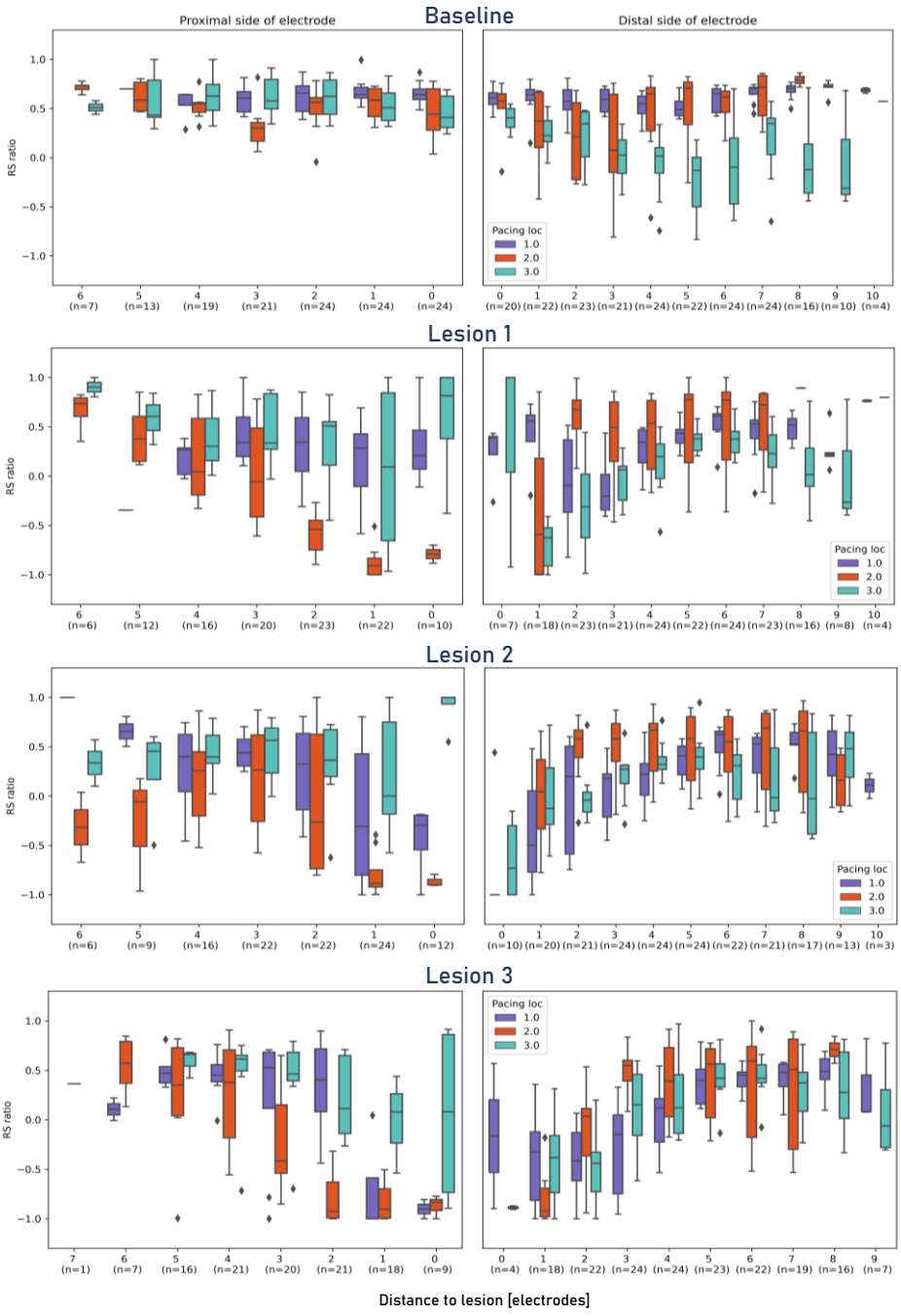

Figure 28 The change of the R/S ratio (y-axis) in relation to the distance from the ablation lesion measured in electrodes (x-axis). The inter-electrode distance is 2 mm. It is noted on how many values the boxplot is based under the x-axis. The maximum value of n is 24. Missing values can be due to malfunctioning electrodes, electrically silent electrodes, short double potentials, fractionated potentials, and some long double potentials. The R/S ratios of mapping location H3 in subject N6 are shown. The left subplots show the site proximal of the ablation lesion and the right subplots the distal side.

Discussion

Key findings

To the best of our knowledge, this is the first study to investigate the acute impact of various stages of surgical ablation on cardiac EGM characteristics and activation patterns with unipolar high-resolution mapping, in three DCD porcine slaughterhouse hearts. The main findings were:

1. A significant increase in CT was seen after one application of RF energy. The CT across the ablation lesion did not change significantly between different stages of continuity and transmurality of the ablation lesion. However, the continuous lesion parts showed a less steep initial increase from baseline to lesion 1, after which the increase gradually continued, whereas the parts without conduction gaps showed a steeper initial increase after which a more stable level of CTs was reached.

2. The potential voltage significantly decreases at the lesion and in its border zone after only one RF application, and the decrease is significantly smaller when there is a conduction gap in the ablation line. Overall, the potential voltage decreased significantly by 84% from baseline to the complete lesion.

3. The potential slope became significantly less steep with one RF application, but there are no clear differences between the sites with and without intentional conduction gaps in the lesion.

4. The S-wave amplitude was predominant at baseline and with a larger distance from the ablation lesion, whereas loss of the S-wave was observed with increasing ablation and more proximate to the ablation lesion, with sometimes monophasic R-waves occurring near the ablation lesion.

5. RF energy may impact an area of 16 mm centered around the ablation lesion, although the measured width of the complete ablation lesion (visual) did not exceed 5 mm.

Activation maps and conduction times

The steepest and only significant increase in median CT across the lesion was observed after one application of RF energy. CT did not change significantly between different stages of ablation lesions. However, the conduction gap site showed a less steep initial increase in median CT compared to the non-gap site, 62.5 ms versus 75.2 ms, respectively. Additional applications of RF resulted in a steady increase in median CT at the gap site, whereas non-gap sites had a more stable CT between the different lesions.

When applying RF energy to tissue, prolonged inter-electrode CTs could indicate slow conduction through an incomplete lesion, conduction through deeper layers, or the time delay for the activation wavefront to find a new path around the lesion. Activation maps can help

distinguish between these possibilities by showing the direction of wavefront propagation. In one out of three swine hearts, a focal conduction gap was detected in the activation map of the first lesion, as the wavefront on the opposite side of the ablation lesion originated from the center of the lesion. The gap stretched across a width of two electrodes that showed inter-electrode CTs of 20.5 and 25.5 ms, corresponding to conduction velocities of 9.8 cm/s and 7.8 cm/s, respectively. These values far exceed the predefined threshold for conduction block in the atria of 12 ms, corresponding to a conduction velocity of 17 cm/s [60]. Measuring the cardiac walls, which are three-dimensional structures, in a two-dimensional manner induces measurement inaccuracy. The deeper layers of the RV wall allow for more variability in wavefront propagation directions compared to the thinner atrial wall, invisible at the measured epicardial surface. If conduction gaps are located in deeper tissue layers (intramural gap [59]), the wavefront propagates towards deeper layers before returning to the epicardial surface, traveling a longer distance and thus having a greater conduction velocity than suggested by two-dimensional epicardial mapping. Therefore, although conduction velocities through the atrial and ventricular myocardium are comparable (50-100 cm/s [64-67]), the conduction block threshold defined for the atria is not appropriate for the ventricles.

In the other two swine, possibly no intentional conduction gap was created, despite the rubber piece on the ablation clamp. RF induces coagulation necrosis of targeted myocardium through resistive and conductive heating. RF waves set molecules in the tissue in direct contact with the electrode into motion, causing frictional energy and heat deposition, which conducts through the tissue with temperature exponentially decreasing with distance [68, 69]. Therefore, heat may have dissipated to the area underneath the rubber piece. Another possibility is that slow conduction through the gap was overruled by a faster wavefront around the lesion. Perpendicular pacing is used to overcome this but may not always be effective, especially in thicker tissue.

A fixed or absolute threshold value for CT to identify nontransmural and discontinuous ablation lesions is dependent on many factors such as tissue thickness and the location of the lesion. Our findings suggest that the stability of CT provides valuable information for lesion assessment and that it is easier to obtain and interpret than absolute values. Changes in the median CT with additional RF application are an indicator of a discontinuous lesion. The entire ablation lesion should be mapped to ensure continuity and to localize the origin of wavefronts on activation maps. While a stable CT indicates a lower likelihood of a discontinuous lesion, it does not necessarily confirm that the lesion is transmural. Therefore, the CT should be evaluated in conjunction with other parameters.

Voltage

Unipolar potential voltage depends on multiple factors, like the volume of simultaneously activated cardiac tissue and conduction velocity. A larger volume of simultaneously activated cardiac tissue results in a larger amplitude of unipolar EGMs [61, 70-72]. Also, fast propagating wavefronts are characterized by EGMs with large amplitude [61, 70, 71]. In contrast, unipolar voltage is lower in areas of slow conduction or conduction block [70]. Prior research demonstrated that the normal range for potential voltage in the ventricles is 5-30 mV [73].

A large, significant decrease in potential voltage was observed after the first application of RF energy (43% for the gap site, 58% for the non-gap sites as measured in the area 16 mm centered around the lesion), caused by coagulation necrosis. The first application was stopped if conductance measured by the ablation clamp fell below 2.5 mS or if an ablation time of 40

seconds was reached. Although not histologically verified, the first ablation lesion was assumed to be nontransmural and discontinuous. Huhn et al. (2018) [62] showed a comparable potential voltage reduction after 30 seconds of catheter ablation (40-61%) in three points in the LA. The voltage in the site with a conduction gap was higher, without overlap in IQR, compared to the site without a conduction gap (10.5 mV versus 7.6 mV). The additional delivery of RF caused the voltage of both sites to converge, although the gap site received less ablation. Because the voltage at the site without a conduction gap remained stable, the additional ablation appears to have affected mainly the conduction gap. Another significant decrease in voltage between lesion 2 and 3 was observed at all mapping locations when the lesion was made transmural (60% for the gap site, 61% for the non-gap site). The center of the lesion was most affected, but the border zone is also affected and shows a gradual decrease in voltage with a smaller distance from the lesion. Visually, the maximum lesion width was approximately 5 mm, whereas the severely affected area often extended to a region of 12-16 mm centered around the lesion, most likely due to conductive heating. This border zone is similar to that of Huhn et al. (2018) [62], who showed that voltages decreased in a 14 mm area around the catheter ablation lesion by high-resolution mapping in three point ablations in the LA. Overall, the potential voltage in the lesion and its border zone decreased by 83% and 85% for the gap and non-gap location, respectively. Gepstein et al. (1999) [74] targeted an amplitude reduction of 80% during catheter ablation between the SVC and IVC, which resulted in transmural lesions. Strikingly, not all potential amplitudes in the lesion area reached a value of 0 mV, and our data suggest that this is also not a prerequisite for a complete lesion if certain R/S ratio criteria are met, which we will discuss in more detail in the R/S ratio section of the discussion.

Potential slope

The observed changes in potential voltage are mostly similar to the changes in potential slope, indicating that the slope becomes less steep if voltage decreases, with the effect becoming more pronounced as the distance from the lesion decreases. Typical slope values of ventricular EGMs lay between 2 to 3 V/s and 1 to 2 V/s for atrial EGMs [73]. Overall from baseline to the third lesion, the potential slope became 85% to 88% less steep, for the gap- and non-gap site, respectively. However, the potential slope appears to be less useful in discriminating between continuous and discontinuous lesion parts, as no clear difference in median slope between these was found. The relationship between potential voltage and slope is complex, as the slope is affected by both the voltage and duration of the signal. There are different theories about underlying mechanisms that affect the value of the slope, including the spatial locality of the signal [75], the conduction velocity [70], and the size of the electrode [76]. No literature has been written before on the effect of RF ablation on the slope of a cardiac EGM. Reduction in voltage results in less steep slopes, unless the duration shortens in the same proportions. However, damage to gap junctions during ablation reduces conduction velocity and therefore probably increases signal duration [77, 78]. While duration was not thoroughly analyzed in this study, the potential slope does not appear to provide additional valuable information beyond potential voltage.

R/S ratio

The morphology of EGMs, represented by the relative positive (R-wave) and negative (S-wave) components of unipolar EGMs, contains information about conduction properties and therefore could provide information about lesion characterization [61]. The morphology of unipolar potentials can be regarded as the sum of instantaneous current dipoles of a wavefront, generating a positive deflection when the activation wavefront propagates towards the

electrode and a steeply negative deflection as the wavefront reaches the electrode and propagates away, thereby generating a biphasic RS-wave [61]. When the electrode is located at a site of initial activation, depolarization produces a wavefront that propagates radially away from the electrode, thus generating a monophasic S-wave. In contrast, positive R-waves are characteristic of the termination of the activation wavefront [61]. In the DCD porcine hearts, the S-wave amplitude was predominant at baseline and a larger distance from the ablation lesion. During pacing, we create an artificial pacemaker site in the heart from where activation is initiated, and this was always performed close to either the proximal side or the distal side of the electrode array. Therefore, the predominant S-waves were expected as monophasic S-waves are seen at sites of initial pacing. Furthermore, the S-wave amplitude decreased with more ablation and closer to the ablation lesion, which has previously been associated with conduction block during ablative therapy [61, 79-81]. Right next to the ablation lesion, monophasic R waves were sometimes detected, more often on the pacing side of the lesion than on the opposite side. This is expected, as we pace perpendicular to the ablation lesion, meaning that the wavefront will terminate when encountering a complete line of block created by ablation. This effect was also observed in a study by Otomo et al. (2010) [80] in which they found that loss of the S-wave, eventually leading to a monophasic R-wave, distinguished transmural from nontransmural lesions with a sensitivity and specificity of 100%. However, in our study, the complete disappearance of the S-wave, resulting in a monophasic R-wave, was not as consistent. In some files, the R-wave was more prominent in lesion 1 compared to 2. Also, not all electrodes next to the third ablation lesion, which was supposed to be continuous and transmural, exhibited monophasic R-waves. However, Otomo et al. (2010) [80] only confirmed their findings in thin atrial tissue in the posterior wall of the LA adjacent to the esophagus. Our findings suggest that these criteria cannot be directly translated and applied to thicker tissues like the RV wall or thicker atrial tissue. As RF energy causes heat dissipation and subsequent coagulative necrosis radially from the source, the width of the lesion created by bipolar RF energy will be smaller in the middle of the myocardium. In thinner tissue, the lesion width will be relatively more uniform throughout the whole myocardial wall. Therefore, in thicker tissue, the wavefront still travels towards the thinner part of the lesion, beyond the electrode, resulting in an S-wave.

Strengths

Multi-parameter evaluation approach

The complex nature of evaluating the effectiveness of ablation on cardiac tissue has been widely recognized, and a multitude of studies have been conducted to investigate this topic, predominantly in the field of catheter ablation. Despite extensive research efforts, achieving a 100% success rate of ablation procedures to treat AF has remained elusive. By integrating multiple evaluation parameters, this study offers a nuanced understanding of the complex interplay between ablation and cardiac tissue. This approach represents a step forward in the development of an intra-operative evaluation tool, with the potential to enhance patient outcomes and reduce the burden of AF on the healthcare system.

Unipolar high-resolution mapping

Unipolar mapping offers several advantages over bipolar mapping. The bipolar EGM, which is the product of a voltage difference between two recording electrodes, is commonly used in the clinic as it contains local information from the area of the myocardium at the catheter tip

between two electrodes. Because two unipolar EGMs, measured at the two poles, are subtracted to create a bipolar EGM, bipolar EGMs are less susceptible to noise and far-field signals. Unipolar EGMs are derived by an electrode positioned in the heart and an indifferent electrode located at an infinite distance. Therefore, the unipolar EGMs reflect the cardiac electrical activity of the tissue surrounding the recording electrode which decreases with distance. They have the benefit over bipolar EGMs that it carries additional information about the progression of the wavefront and remote activations, which are independent of the electrode orientation and wavefront direction [61, 79]. Low-voltage areas are highly determined by their morphology, but these are currently not fully classified in clinical practice with the bipolar EGMs. Unipolar EGMs provide additional helpful information about R/S ratios [61]. Also, in a study by Yavin et al. (2023) [59] they showed in 15 swine with an atrial intercaval ablation line with an intentional gap that unipolar voltage had a higher sensitivity to detect intramural-epicardial gaps compared to bipolar voltage (93% versus 14%, respectively) when mapping from the endocardium. Sensitivity between unipolar and bipolar EGMs was comparable for areas with transmural scar and endocardial gaps. This study highlights the limitation of bipolar voltage mapping to detect deep layers of viable myocardium. Even in thin-walled atria, a submillimeter layer of endocardial collagen served as an insulator for the bipolar measurement, masking electrical activity occurring just 1 to 2 mm away. The attenuating effect of scar on bipolar EGMs was already previously reported for the ventricles [82]. Therefore, the unipolar mapping configuration used in this study allowed a more accurate analysis of transmurality and intra-mural or endocardial gaps.

Controlled conditions

EVHP provides an opportunity to study EGM characteristics in a controlled environment. Although results eventually should be translated to clinical data obtained during Maze surgery, this controlled setup allowed extensive examination of different degrees of lesions, whereas this would not be possible during Maze surgery, for ethical and temporal considerations. Extension of the surgical procedure for research purposes should be kept to a minimum. The comprehensive research on EVHP guides subsequent clinical research by prescribing the parameters to be studied, the structure of the protocol, and the EGM characteristics of complete ablation.

Limitations and recommendations

The main limitation of this study is that the experiments were conducted on the RV, while Maze surgery is executed on the atria. This was a choice made for practical reasons, as the atria did not always restart after reperfusion of the heart. Important differences between the atria and RV in light of the research purposes are the thicker wall and the larger potential voltages. The effect of the thicker wall was already mentioned a few times in the discussion. It might impact the CT as waves can propagate through deeper layers and thus impacts our threshold values for conduction block. Both the atria and ventricles are three-dimensional structures that we try to describe by measuring them in a two-dimensional manner, however, as the wall thickness increases, the misfit of the two-dimensional approach becomes more pronounced. However, as the wall thickness of the atria are variable and also exhibits thicker parts of myocardium, it is valuable to know how wall thickness impacts electrophysiological parameters. Also, the AtriCure ablation clamp was not designed for the thicker ventricular wall. One application of RF energy, which AtriCure states results in a transmural lesion, appears to be not enough for the ventricles. However, in the hospital, they also apply a lot more ablation than advised by

the AtriCure guideline to the atria due to uncertainty about which settings result in a complete lesion. Therefore, in future research, electrophysiological parameters should be correlated with the conductance measurement shown by AtriCure's ASU, to provide an evidence-based guideline and target for complete ablation lesions. Furthermore, although the voltages in the ventricles are higher, some comparable values of percentage potential amplitude reduction in the atria have been found in the literature, leading to transmural lesions [62, 74].

In addition, several differences exist between the conduction system of the swine heart compared to that of humans, of which the Purkinje-ventricular junctions might be of importance. This connects the Purkinje fibers to the ventricular myocardium transmurally, almost reaching the epicardium, while in humans these junctions are only identified subendocardial. This results in simultaneous activation of the endocardium and epicardium in swine, and also, conduction velocity measured at the epicardium may be higher as we measure close to the Purkinje fibers [83, 84]. However, not all types of animals are available for research due to ethical considerations or high costs, and each animal model has its own limitations. Porcine hearts are the most commonly used animal model to study cardiac electrophysiology and arrhythmias because they share many similarities with the human heart in terms of size, anatomy, and physiology, and they are relatively easy to obtain, and therefore seem a valid choice for the type of research that was conducted [83].

Furthermore, only an acute evaluation of the lesion was performed. Previous studies have indicated that acute electrical isolation is not a reliable indicator of permanent electrical isolation because of local tissue edema caused by ablation, which may mask incomplete lesions, and reversibly damaged myocytes [79, 85, 86]. To unmask dormant conduction that could lead to reconnection, waiting periods of 30 to 60 minutes and adenosine tests are often used in the EP laboratory [86-90]. It is recommended that adenosine be administered at least 20 minutes after RF delivery to ensure proper function [91]. Due to time constraints, a waiting period could not be implemented in our study as multiple experiments had to be conducted in a single day. Although this could be considered a limitation, it is important to recognize that this reflects a real clinical scenario since such long waiting periods are also not feasible during cardiac surgery, as the duration of the procedure should be limited to avoid complications.

Another limitation is the lack of histological examination of the ablation lesions, which precludes definitive conclusions about the transmurality and continuity of the lesions. However, the current experimental design would have allowed histological examination of the last ablation lesion only, because three lesions were subsequently created at the same location. In this way, it was excluded that the changes between the different lesion stages were confounded by different tissue characteristics. Nevertheless, it is recommended for future studies to histologically verify the last created ablation lesion.

Lastly, we recommend to analyze measurements taken simultaneously from the epicardium and endocardium of the heart (epi-endo mapping). This could reveal information about epi-endo asynchrony and whether and how it is affected by ablation. For example, it could provide information on whether a conduction block detected on one side of the heart still allows for a preserved opposite layer with other EGM characteristics.

Clinical relevance

To the best of our knowledge, this is the first study to provide a comprehensive analysis of the impact of various stages of surgical ablation on cardiac EGM characteristics and activation patterns using unipolar high-resolution mapping in ex vivo perfused porcine hearts. The ultimate goal is to set up an intra-operative evaluation tool, to avoid post-maze gap-related ATs. The comprehensive evaluation in the EP laboratory stands contrary to the evaluation of lesions during cardiac surgery, which ranges from no evaluation at all to only a pacing maneuver, as no guidelines are present. As cardiothoracic surgeons have little experience with electrophysiology, the intra-operative evaluation tool should be designed in an intuitive and easy-to-use way, to make it accessible and stimulate electrophysiological evaluation. The findings of this study, which demonstrate the efficacy of high-resolution mapping for guiding ablation procedures and identifying critical regions for reconduction, are translational to clinical practice and have the potential to significantly improve patient outcomes by reducing the incidence of post-maze gap-related ATs. Therefore, this study marks the onset of a promising development and will provide valuable support to surgeons during Maze procedures in the future and can aid in the patient-tailored management of AF.

Conclusion

Ablation lesions are characterized by a prolongation of the conduction time across the lesion, decreased potential voltages with a gradual decrease in the border zone, and a loss of S-wave amplitude of single potentials or long double potentials. The extent to which these parameters are affected depends on the amount of radiofrequency energy applied, but a significant change is seen after the first radiofrequency delivery, although this does not yet result in a complete lesion. A stable conduction time combined with an activation wavefront propagating around the ablation lesion makes discontinuity of ablation lesions unlikely, but cannot rule out nontransmurality. The potential voltage appears to be sensitive to both discontinuity and nontransmurality and can therefore be used as a complementary parameter. A decrease in potential voltage of 84% in the border zone leads to a transmural and continuous lesion. The potential voltage does not necessarily have to reach values of 0 mV when interpreted in conjunction with the R/S ratio, since a voltage that is brought about by a monophasic R-wave also indicates termination of the wavefront propagation and thus a complete lesion. A small S-wave (instead of a monophasic R-wave) does not exclude the possibility of a transmural lesion in thicker tissue. The slope of the potentials does not add much value to lesion evaluation. The combination of conduction time, potential voltage, and R/S ratio in one evaluation tool could help detect incomplete surgical ablation lesions in the individual patient during Maze surgery, potentially reducing post-maze gap-related atrial tachyarrhythmias and thus improving long-term success rates.

References

1. Hindricks G, Potpara T, Dagres N, Arbelo E, Bax JJ, Blomström-Lundqvist C, et al. 2020 ESC Guidelines for the diagnosis and management of atrial fibrillation developed in collaboration with the European Association for Cardio-Thoracic Surgery (EACTS): The Task Force for the diagnosis and management of atrial fibrillation of the European Society of Cardiology (ESC) Developed with the special contribution of the European Heart Rhythm Association (EHRA) of the ESC. European Heart Journal. 2020;42(5):373-498.
2. Kik C, Bogers AJ. Maze Procedures for Atrial Fibrillation, From History to Practice. Cardiology research. 2011;2(5):201-7.
3. Lee R. Atrial fibrillation: Surgical ablation. UpToDate 2022.
4. Amin A, Houmsse A, Ishola A, Tyler J, Houmsse M. The current approach of atrial fibrillation management. Avicenna J Med. 2016;6(1):8-16.
5. Khiabani AJ, MacGregor RM, Bakir NH, Manghelli JL, Sinn LA, Maniar HS, et al. The long-term outcomes and durability of the Cox-Maze IV procedure for atrial fibrillation. The Journal of Thoracic and Cardiovascular Surgery. 2022;163(2):629-41.
6. Damiano Jr RJ, Schwartz FH, Bailey MS, Maniar HS, Munfakh NA, Moon MR, et al. The Cox maze IV procedure: predictors of late recurrence. The Journal of Thoracic and Cardiovascular Surgery. 2011;141(1):113-21.
7. Conte G, Soejima K, de Asmundis C, Bruno J, Cattaneo F, Chierchia GB, et al. High-density mapping in patients undergoing ablation of atrial fibrillation with the fourth-generation cryoballoon and the new spiral mapping catheter. Europace. 2020;22(11):1653-8.
8. Ganesan AN, Shipp NJ, Brooks AG, Kuklik P, Lau DH, Lim HS, et al. Long-term Outcomes of Catheter Ablation of Atrial Fibrillation: A Systematic Review and Meta-analysis. Journal of American Heart Association. 2013;2(2).
9. Andrade JG, Khairy P, Guerra PG, Deyell MW, Rivard L, Macle L, et al. Efficacy and safety of cryoballoon ablation for atrial fibrillation: A systematic review of published studies. Heart Rhythm. 2011;8(9):1444-51.
10. van Brabandt H, Neyt M, Devos C. Effectiveness of catheter ablation of atrial fibrillation in Belgian practice: a cohort analysis on administrative data. Europace. 2013;15(5):663-8.
11. Arbelo E, Brugada J, Hindricks G, Maggioni AP, Tavazzi L, Vardas P, et al. The atrial fibrillation ablation pilot study: a European Survey on Methodology and results of catheter ablation for atrial fibrillation conducted by the European Heart Rhythm Association. European Heart Journal. 2014;35(22):1466-78.
12. Kim JH, Kim JS, Kim TS. Epicardial thoracoscopic ablation versus endocardial catheter ablation for management of atrial fibrillation: a systematic review and meta-analysis. Interdisciplinary CardioVascular and Thoracic Surgery. 2016;22(6):729-37.
13. Gammie JS, Haddad M, Milford-Beland S, Welke KF, Ferguson TB, O'Brien SM, et al. Atrial fibrillation correction surgery: lessons from the Society of Thoracic Surgeons National Cardiac Database. The Annals of Thoracic Surgery. 2008;85(3):909-14.
14. Kajiyama T, Kondo Y, Ueda M, Nakano M, Nakano M, Watanabe M, et al. Catheter ablation of atrial tachyarrhythmias after a Maze procedure: A single center experience. Journal of Cardiology Cases. 2019;19:89-92.
15. Kataoka S, Kato K, Tanaka H, Tejima T. Atrial tachycardia originating from an incompletely isolated box lesion in a patient undergoing thoracoscopic left atrial appendectomy and surgical ablation for long-standing persistent atrial fibrillation. Journal of Cardiology Cases. 2018;18:25-8.

16. Winkle RA, Fleming W, Hardwin Mead R, Engel G, Kong MH, Salcedo J, et al. Catheter ablation for failed surgical maze: comparison of cut and sew vs. non-cut and sew maze. Journal of Interventional Cardiac Electrophysiology. 2019;55:183-9.
17. Suzuki K, Miyamoto K, Ueda N, Nakajima K, Kamakura T, Wada M, et al. Relationship between electrical gaps after Maze procedure and atrial tachyarrhythmias and ablation outcomes after cardiac surgery and concomitant Maze procedure. Heart and Vessels. 2021;36(5):675-85.
18. Gopinathannair R, Mar PL, Rizwan Afzal M, Biase LD, Tu Y, Lakkireddy T, et al. Atrial Tachycardias After Surgical Atrial Fibrillation Ablation: Clinical Characteristics, Electrophysiological Mechanisms, and Ablation Outcomes From a Large, Multicenter Study. JACC: Clinical Electrophysiology. 2017;3(8):865-74.
19. Huo Y, Schoenbauer R, Richter S, Rolf S, Sommer P, Arya A, et al. Atrial arrhythmias following surgical AF ablation: Electrophysiological findings, ablation strategies, and clinical outcome. Journal of cardiovascular electrophysiology. 2014;25(7):725-38.
20. Magnano AR, Argenziano M, Dizon JM, Vigilance D, Williams M, Yegen H, et al. Mechanisms of atrial achyarrhythmias following surgical atrial fibrillation ablation. Journal of cardiovascular electrophysiology. 2006;17(4):366-73.
21. Akar JG, Al-Chekakie MO, Hai A, Brysiewicz N, Porter M, Varma N, et al. Surface electrocardiographic patterns and electrophysiologic characteristics of atrial flutter following modified radiofrequency MAZE procedures. Journal of cardiovascular electrophysiology. 2007;18(4):349-55.
22. Nakai K, Kashiwa A, Kunitomi A, Matsuoka S. Conduction gap mapping of linear ablation lesions with high-density mapping. J Cardiovasc Electrophysiol. 2020;31(8):1953-63.
23. Tahara M, Kato R, Ikeda Y, Goto K, Asano S, Mori H, et al. Differential Atrial Pacing to Detect Reconnection Gaps After Pulmonary Vein Isolation in Atrial Fibrillation. International heart journal. 2020;61(3):503-9.
24. Xie H, Guo X, Yang J, Chen Y, Cao Z, Sun Q, et al. Novel Clue to Locate Conduction Gaps in the Pulmonary Vein Isolation Ablation Line. Frontiers in cardiovascular medicine. 2021;8:622483.
25. Wenink KM. Electrophysiological Evaluation of the Continuity and Transmurality of Catheter Ablation Lesions in Atrial Fibrillation Patients: A Systematic Review. 2022.
26. de Groot NMS, Shah D, Boyle PM, Anter E, Clifford GD, Deisenhofer I, et al. Critical appraisal of technologies to assess electrical activity during atrial fibrillation: a position paper from the European Heart Rhythm Association and European Society of Cardiology Working Group on eCardiology in collaboration with the Heart Rhythm Society, Asia Pacific Heart Rhythm Society, Latin American Heart Rhythm Society and Computing in Cardiology. Europace. 2021;24(2):313-30.
27. Maesen B, Zeemering S, Afonso C, Eckstein J, Burton RA, van Hunnik A, et al. Rearrangement of atrial bundle architecture and consequent changes in anisotropy of conduction constitute the 3-dimensional substrate for atrial fibrillation. Circ Arrhythm Electrophysiol. 2013;6(5):967-75.
28. Olshansky B, Arora R. Mechanisms of atrial fibrillation. UpToDate 2022.
29. Kik C, Mouws E, Bogers A, de Groot NMS. Intra-operative mapping of the atria: the first step towards individualization of atrial fibrillation therapy? Expert Rev Cardiovasc Ther. 2017;15(7):537-45.
30. Houben RP, Allessie MA. Processing of intracardiac electrograms in atrial fibrillation. Diagnosis of electropathological substrate of AF. IEEE Eng Med Biol Mag. 2006;25(6):40-51.
31. Goodacre S, McLeod K. ABC of clinical electrocardiography: Paediatric electrocardiography. BMJ. 2002;324(7350):1382-5.
32. Heemstra HE, Nieuwlaat R, Meijboom M, Crijns HJ. The burden of atrial fibrillation in the Netherlands. Neth Heart J. 2011;19(9):373-8.
33. Verbiest-van Gurp N, van Bladel PJM, van Kesteren HAM, Erkens PM, Stoffers H. Current practice of Dutch cardiologists in detecting and diagnosing atrial fibrillation: results of an online case vignette study. Neth Heart J. 2017;25(10):567-73.
34. de Boer AR, Bots ML, van Dis I, Vaartjes I, Visseren FLJ. Cijfers over incidentie, prevalentie, ziekte en sterfte.2019.
35. Kumar K. Atrial fibrillation: Overview and management of new-onset atrial fibrillation. UpToDate 2022.
36. January CT, Wann LS, Alpert JS, Calkins H, Cigarroa JE, Cleveland JC, et al. 2014 AHA/ACC/HRS Guideline for the Management of Patients With Atrial Fibrillation A Report of the American College

of Cardiology/American Heart Association Task Force on Practice Guidelines and the Heart Rhythm Society. Circulation 2014;130(23):2071-104.
37. Cheniti G, Vlachos K, Pambrun T, Hooks D, Frontera A, Takigawa M, et al. Atrial Fibrillation Mechanisms and Implications for Catheter Ablation. Frontiers in Physiology. 2018;9.
38. Allessie MA, Ausma J, Schotten U. Electrical, contractile and structural remodeling during atrial fibrillation. Cardiovascular Research. 2002;54(2):230-46.
39. Wijffels M, Kirchhof CJHJ, Dorland R, Allessie MA. Atrial Fibrillation Begets Atrial Fibrillation. Circulation. 1995;92(7):1954-68.
40. Barbhaiya CR, Aizer A, Knotts R, Bernstein S, Park D, Holmes D, et al. Simultaneous pace-ablate during CARTO-guided pulmonary vein isolation with a contact-force sensing radiofrequency ablation catheter. J Interv Card Electrophysiol. 2019;54(2):119-24.
41. Mochizuki A, Nagahara D, Kamiyama N, Fujito T, Miura T. Revaluation of the Significance of Demonstrable Exit Block After Radiofrequency Pulmonary Vein Isolation. Circ Rep. 2020;2(4):218-25.
42. Malik R, Malik B, Hunter TD. Touch-up and recurrence rates after voltage mapping for verification of pulmonary vein isolation following cryoablation of paroxysmal atrial fibrillation. J Interv Card Electrophysiol. 2019;56(3):307-12.
43. Ruiz-Granell R, Ballesteros G, Andreu D, Erkiaga A, Ferrero-De-Loma-Osorio A, Ramos P, et al. Differences in scar lesion formation between radiofrequency and cryoballoon in atrial fibrillation ablation: a comparison study using ultra-high-density mapping. Europace. 2019;21(2):250-8.
44. Chin SH, O'Brien J, Epicoco G, Peddinti P, Gupta A, Modi S, et al. The feasibility and effectiveness of a streamlined single-catheter approach for radiofrequency atrial fibrillation ablation. J Arrhythm. 2020;36(4):685-91.
45. Sousa P, Barra S, Puga L, Sousa C, Elvas L. Extended early meets late for assessment of conduction block along an ablation line. Journal of interventional cardiac electrophysiology : an international journal of arrhythmias and pacing. 2022;63(2):431-40.
46. Chen W, Lo L, Tsai W, Lin Y, Chang S, Hu Y, et al. Application of dynamic display technology to identify gaps after pulmonary vein isolation in catheter ablation of atrial fibrillation. Journal of cardiology. 2022.
47. Viola N, Williams MR, Oz MC, Ad N. The technology in use for the surgical ablation of atrial fibrillation. Seminars in Thoracic and Cardiovascular Surgery. 2002;14(3):198-205.
48. Damiano Jr RJ. Alternative energy sources for atrial ablation: judging the new technology. The Annals of Thoracic Surgery. 2003;75(2):329-30.
49. Lesion Set Options 2019 [updated June 10, 2019. Available from: https://www.afibsurgeons.org/maze-procedure/lesion-set-radiofrequency-cryo/.
50. Weimar T, Bailey MS, Watanabe Y, Marin D, Maniar HS, Schuessler RB, et al. The cox-maze IV procedure for lone atrial fibrillation: A single center experience in 100 consecutive patients. Journal of Interventional Cardiac Electrophysiology. 2011;31(1):47-54.
51. Henn MC, Lancaster TS, Miller JR, Sinn LA, Schuessler RB, Moon MR, et al. Late outcomes after the Cox maze IV procedure for atrial fibrillation. The Journal of Thoracic and Cardiovascular Surgery. 2015;150(5):1168-76.
52. Knottenbelt M. Langendorff vs. Working Heart Perfusion – What's the difference? 2019 [updated September 12, 2019. Available from: https://www.adinstruments.com/blog/langendorff-vs-working-heart-perfusion.
53. Langmuur SJJ, Amesz JH, Veen KM, Bogers AJJC, Manintveld OC, Taverne YJHJ. Normothermic Ex Situ Heart Perfusion With the Organ Care System for Cardiac Transplantation: A Meta-Analysis. Transplantation. 2022;106(9):1745-53.
54. Beuth J, Falter F, R. P, V. R, Badiwala M, Meineri M. New Strategies to Expand and Optimize Heart Donor Pool: Ex Vivo Heart Perfusion and Donation After Circulatory Death: A Review of Current Research and Future Trends. Cardiovascular and Thoracic Anesthesiology. 2019;128(3):406-13.
55. Amesz JH, Langmuur SJJ, van Schie MS, Taverne YJHJ. Production of living myocardial slices from circulatory death hearts after ex vivo heart perfusion. The Journal of Thoracic and Cardiovascular Surgery. 2022;14(13):128-30.
56. Isolator Synergy Ablation System - The Only FDA-Approved Surgical Device to Treat Atrial Fibrillation During Heart Surgery. In: AtriCure, editor.: AtriCure. p. 4.

57. Isolator Synergy Clamps (OLL2/OSL2): AtriCure; [Available from: https://www.atricure.com/healthcare-professionals/therapies/concomitant-surgical-ablation/isolator-synergy-clamps-OLL2-OSL2.
58. Ablation Sensing Unit and Switch Matrix ASU and ASB: Astemed; [Available from: https://astemed.com/product/operating-theatre/ablation-sensing-unit-and-switch-matrix-asu-and-asb/.
59. Yavin H, Younis A, Zilberman I, Krywanczyk A, Bubar ZP, Higuchi K, et al. Atrial Endocardial Unipolar Voltage Mapping for Detection of Viable Intramural Myocardium: A Proof-of-Concept Study. Circulation: Arrhythmia and Electrophysiology. 2023;16(1).
60. Allessie MA, de Groot NMS, Houben RP, Schotten U, Boersma E, Smeets JL, et al. Electropathological substrate of long-standing persistent atrial fibrillation in patients with structural heart disease: longitudinal dissociation. Circulation: Arrhythmia and Electrophysiology. 2010;3(6):606-15.
61. van Schie MS, Starreveld R, Roos-Serote MC, Taverne YJHJ, van Schaagen FRN, Bogers AJJC, et al. Classification of sinus rhythm single potential morphology in patients with mitral valve disease. Europace. 2020;22(10):1509-19.
62. Huhn O, Pollnow S, Unger L, Dössel O, Oesterlein T, Luik A, et al. High-density Mapping Reveals Short-term Reversibility of Atrial Ablation Lesions. Current Directions in Biomedical Engineering. 2018;4(1):385-8
63. Kharbanda RK, van Schie MS, Ramdat Misier NL, Wesselius FJ, Zwijnenburg RD, van Leeuwen WJ, et al. In-vivo Sino-Atrial Node Mapping in Children and Adults With Congenital Heart Disease. Frontiers in Pediatrics. 2022;10.
64. van Schie MS, Heida A, Taverne YJHJ, Bogers AJJC, de Groot NMS. Identification of local atrial conduction heterogeneities using high-density conduction velocity estimation. Europace. 2021;23(11):1815-25.
65. Hoogendijk M. Differential diagnosis of broad complex tachycardias Erasmus Medical Center, Rotterdam 2020.
66. Kléber AG, Janse MJ, Wilms-Schopmann FJ, Wilde AA, Coronel R. Changes in conduction velocity during acute ischemia in ventricular myocardium of the isolated porcine heart. Circulation. 1986;73(1):189-98.
67. Anter E, Kleber AG, Rottmann M, Leshem E, Barkagan M, Tschabrunn CM, et al. Infarct-Related Ventricular Tachycardia: Redefining the Electrophysiological Substrate of the Isthmus During Sinus Rhythm. JACC: Clinical Electrophysiology. 2018;4(8):1033-48.
68. Chinitz JS, Michaud GF, Stephenson K. Impedance-guided Radiofrequency Ablation: Using Impedance to Improve Ablation Outcomes. The Journal of Innovations in Cardiac Rhythm Management 2017;8(10):2868-73.
69. Hong K, Georgiades C. Radiofrequency ablation: mechanism of action and devices. Journal of Vascular and Interventional Radiology. 2010;21(8):179-86.
70. van Schie MS, Kharbanda RK, Houck CA, Lanters EAH, Taverne YJHJ, Bogers AJJC, et al. Identification of Low-Voltage Areas: A Unipolar, Bipolar, and Omnipolar Perspective. Circ Arrhythm Electrophysiol. 2021;14(7):e009912.
71. Spach MS, Miller WT, Miller-Jones E, Warren RB, Barr RC. Extracellular potentials related to intracellular action potentials during impulse conduction in anisotropic canine cardiac muscle. Circulation Research. 1979;45(2):188-204.
72. de Groot NMS, Schalij MJ, Zeppenfeld K, Blom NA, van der Velde ET, van der Wall EE. Voltage and activation mapping: how the recording technique affects the outcome of catheter ablation procedures in patients with congenital heart disease. Circulation. 2003;108(17):2099-106.
73. Swerdlow CD, Gillberg JM, Khairy P. Sensing and Detection In: Ellenbogen KA, Kay GN, Lau C, Willkoff BL, editors. Clinical Cardiac Pacing, Defibrillation, and Resynchronization Therapy. Third ed: Saunders 2007. p. 75-160.
74. Gepstein L, Hayam G, Shpun S, Cohen D, Ben-Haim SA. Atrial linear ablations in pigs. Chronic effects on atrial electrophysiology and pathology. Circulation. 1999;100(4):419-26.
75. Bera D, Narasimhan C. Electrograms in redo-ablations: Near-field or far-field or both? Indian Pacing and Electrophysiology Journal. 2022;22(1).
76. Abdi B, van Schie MS, de Groot NMS, Hendriks RC. Analyzing the effect of electrode size on electrogram and activation map properties. Computers in Biology and Medicine. 2021;132.

77. Elvan A, Huang X, Pressler ML, Zipes DP. Radiofrequency Catheter Ablation of the Atria Eliminates Pacing-Induced Sustained Atrial Fibrillation and Reduces Connexin 43 in Dogs. cIRCULATION. 1997;96(5).
78. Jongsma HJ, Wilders R. Gap junctios in Cardiovascular Disease. Circulation Research. 2000;86(12).
79. Kumar S, Michaud GF. Unipolar electrogram morphology to assess lesion formation during catheter ablation of atrial fibrillation: successful translation into clinical practice. Circulation: Arrhythmia and Electrophysiology. 2013;6(6):1050-2.
80. Otomo K, Uno K, Fujiwara H, Isobe M, Iesaka Y. Local unipolar and bipolar electrogram criteria for evaluating the transmurality of atrial ablation lesions at different catheter orientations relative to the endocardial surface. Heart Rhythm. 2010;7(9):1291-300.
81. Villacastin J, Almendral J, Arenal A, Castellano NP, Gonzalez S, Ortiz M, et al. Usefulness of Unipolar Electrograms to Detect Isthmus Block After Radiofrequency Ablation of Typical Atrial Flutter. Circulation. 2000;102(25):3080-5.
82. Miller JM, Tyson GS, HargroveIII WC, Vassallo JA, Rosenthal ME, Josephson ME. Effect of Subendocardial Resection on Sinus Rhythm Endocardial Electrogram Abnormalities. Circulation. 1995;91(9):2385-91.
83. Levolas PP, Kostomitsopoulos NG, Xanthos TT. A Comparative Anatomic and Physiologic Overview of the Porcine Heart. Journal of the American Association for Laboratory Animal Science. 2014;53(5):432-8.
84. Tomaselli GF, Rubart M, Zipes DP. Mechanisms of Cardiac Arrhythmias. Braunwald's Heart Disease: a Textbook of Cardiovascular Medicine, 2-Volume Set: Elsevier 2019.
85. Vroomen M, Maesen B, Luermans JL, Maessen JG, Crijns HJ, La Meir M, et al. Epicardial and Endocardial Validation of Conduction Block After Thoracoscopic Epicardial Ablation of Atrial Fibrillation. Innovations. 2020;15(6):525-31.
86. Sze E, Bahnson TD. Pulmonary Vein Isolation Lesion Set Assessment During Radiofrequency Catheter Ablation for Atrial Fibrillation. J Innov Card Rhythm Manag. 2017;8(2):2602-11.
87. Martins RP, Galand V, Behar N, Daubert JC, Mabo P, Leclercq C, et al. Localization of Residual Conduction Gaps After Wide Antral Circumferential Ablation of Pulmonary Veins. JACC: Clinical Electrophysiology. 2019;5(7):753-65.
88. El Haddad M, Taghji P, Phlips T, Wolf M, Demolder A, Choudhury R, et al. Determinants of Acute and Late Pulmonary Vein Reconnection in Contact Force–Guided Pulmonary Vein Isolation Identifying the Weakest Link in the Ablation Chain. Circ Arrhythm Electrophysiol. 2017;10(4).
89. Wang N, Phan S, Kanagaratnam A, Kumar N, Phan K. Adenosine Testing After Atrial Fibrillation Ablation: Systematic Review and MetaAnalysis. Heart, Lung and Circulation. 2018;27:601-10.
90. McLellan AJA, Kumar S, Smith C, Morton JB, Kalman JM, Kistler PM. The role of adenosine following pulmonary vein isolation in patients undergoing catheter ablation for atrial fibrillation: a systematic review. Journal of Cardiovascular Electrophysiology. 2013;24(7):742-51.
91. Calkins H, Hindricks G, Cappato R, Kim YH, Saad EB, Aguinaga L, et al. 2017 HRS/EHRA/ECAS/APHRS/SOLAECE expert consensus statement on catheter and surgical ablation of atrial fibrillation: Executive summary. Heart Rhythm. 2017;14(10):e445-e94.

Appendices

Appendix A: Experimental protocol

CONFIDENTIAL APPENDIX

The confidential appendix is accessible only to the graduation committee. These pages are intentionally left blank.

Appendix B: Clinical mapping protocol

CONFIDENTIAL APPENDIX

The confidential appendix is accessible only to the graduation committee. These pages are intentionally left blank.

Appendix C: Series of EVHP experiments

This section contains a logbook of all eight EVHP experiments conducted. Three experiments that were successful and fitted in the time schedule of this master's thesis were included for analysis. Subjects N2, N3, and N6 were included.

Table C1 Details on ex vivo heart perfusion experiments

Subject	Animal	Date	Measured	RV mapping complete?	Intrinsic rhythm	Pacing rate [bpm]	Pacing ampl. [mA]	Warm ischemic time	Total ischemic time	Lesion width	Remarks	Incl.	Reason	Improvements for next experiment
N1	Antelope	28-07-22	RA	Not executed								No	RV not measured + Antelope instead of swine + first tryout of experiment	Mark epicardial spatula + use bipolar pacemaker wire that can be stitched to ensure same pacing location
N2	Swine	18-10-22	RV	No*	No	100	5	3:58	1:56:19	Inferior 4-5 mm, superio r mm		Yes		Mark gap site + mark 64 epicardial electrodes on epic-end spatula + use a reference to map the same location each time
N3	Swine	25-10-22	RV + LA	Yes	No	100	5	4:00	1:55:28	/		Yes		Note ablation times + store tissue for histological examination
N4	Swine	08-11-22	RV	Yes	No	100	2/1	4:00	2:03:10	3-4 mm	Cold NaCl forgotten at decoupling	No	Pacing location 2 was biventricular	
N5	Swine	22-11-22	RV	Yes	Yes	100	1	4:12	2:10:10	4 mm		No	Pacing location 2 was biventricular	Make sure pacing location 2 is not biventricular paced
N6	Swine	29-11-22	RV + LA	Yes	Yes	100	2	3:58	1:56:15	/		Yes		Check electrodes everytime before connecting them
N7	Swine	06-12-22	RV + LA	Yes	Yes	100	7	Unknown	Unknown	3-4 mm		No	Too late in graduation timeline	
N8	Swine	13-12-22	RV + LA	No **	Yes	100	1/2	6:15	2:04:41	/	Heart not decoupled because of failure of first experiment. Intrinsic rhythm, but ventricular rhythm after first lesion. Missing mapping locations due to high placement of incision.	No	Too late in graduation timeline	

* Measurements of H1p1, H1p2, H3p1 and H3p2 of the baseline measurement and lesion 1 are missing.
** Measurements of all H3 mapping locations are missing.

Appendix D: Supplemental figures and tables

Conduction times

Table D1 Descriptive statistics of conduction times across the ablation lesion in milliseconds (ms). Locations H1 and H3 were used to analyze the difference in conduction times between different stages of ablation lesions without an intentional conduction gap.

		Median (IQR)			
Subject	Location	Baseline	Lesion 1	Lesion 2	Lesion 3
N3	H1p1	5.0 (4.5-6.5)	95.5 (86.0-103.5)	112.5 (105.5-123.8)	112.4 (98.6-121.9)
N3	H1p2	3.5 (3.1-4.2)	51.0 (35.1-54.5)	59.0 (55.0-63.8)	58.5 (57.0-61.8)
N3	H3p1	2.5 (2.2-3.8)	103.5 (94.0-133.2)	128.5 (126.1-135.0)	108.4 (89.0-137.8)
N3	H3p2	3.5 (1.8-8.2)	82.0 (76.0-87.9)	86.5 (72.0-98.4)	87.9 (83.8-92.6)
N6	H1p1	3.8 (3.1-4.4)	68.0 (54.8-94.0)	97.5 (77.9-126.9)	83.2 (75.0-103.1)
N6	H1p2	4.0 (1.5-4.5)	75.5 (71.2-88.8)	101.2 (94.8-111.0)	113.5 (102.5-115.4)
N6	H1	4.0 (2.9-5.8)	37.5 (28.0-55.4)	82.1 (62.4-87.4)	75.0 (58.8-83.1)
N6	H3p1	3.9 (1.6-5.1)	121.9 (117.9-130.3)	110.0 (100.5-126.0)	115.4 (112.4-124.1)
N6	H3p2	1.0 (1.0-2.0)	110.0 (106.5-114.0)	96.5 (95.4-103.0)	95.5 (91.4-105.2)
N6	H3	3.0 (2.1-4.4)	34.5 (33.8-42.0)	40.8 (27.6-44.6)	26.2 (18.9-38.5)
Median	All	3.6 (3.1-4.0)	78.8 (55.2-101.5)	97.0 (83.2-107.8)	91.7 (77.0-111.4)

Table D2 Descriptive statistics of conduction times across the ablation lesion in milliseconds (ms). Location H2 was used to analyze if there is an effect of a conduction gap in the ablation line on the conduction times. During the first and second lesion a piece of rubber was present on the ablation clamp to create an artificial gap in the conduction line.

		Median (IQR)			
Subject	Location	Baseline	Lesion 1	Lesion 2	Lesion 3
N2	H2p1	2.5 (2.5-2.9)	32.0 (28.2-35.0)	74.2 (68.0-86.2)	123.0 (120.8-126.5)
N2	H2p2	2.9 (2.2-3.5)	47.8 (39.3-52.5)	92.0 (88.8-101.5)	115.0 (105.0-127.1)
N3	H2p1	6.5 (5.2-7.5)	125.8 (113.0-132.8)	140.2 (136.5-151.0)	148.0 (146.8-153.6)
N3	H2p2	2.0 (1.0-3.0)	59.8 (50.4-67.1)	76.4 (67.2-80.8)	78.5 (68.1-84.1)
N6	H2p1	4.5 (4.0-5.8)	172.0 (164.6-175.9)	149.2 (145.5-151.5)	135.2 (125.6-141.4)
N6	H2p2	3.0 (3.0-3.5)	109.0 (106.8-111.2)	96.0 (94.8-98.5)	95.9 (94.2-100.5)
N6	H2	3.5 (2.9-3.8)	65.5 (58.8-71.5)	35.2 (1.2-72.1)	53.8 (44.1-59.9)
	All	3.0 (2.7-4.0)	65.5 (53.8-117.4)	92.0 (75.3-118.1)	115.0 (87.2-129.1

Voltage

Table D3 Descriptive statistics of voltage (peak-to-peak amplitude) measured in milliVolts (mV). Locations H1 and H3 were used to analyze the difference in voltage between different stages of ablation lesions without an intentional gap. An area of 64 electrodes around the ablation lesion, 32 on the proximal and 32 on the distal side, was included in this analysis.

		Median (IQR)			
Subject	Location	Baseline	Lesion 1	Lesion 2	Lesion 3
N3	H1p1	20.8 (18.5-22.3)	16.3 (11.9-19.9)	10.1 (7.4-14.3)	4.2 (2.0-8.9)
N3	H1p2	22.6 (20.8-24.4)	15.4 (8.1-21.4)	9.2 (3.5-17.8)	3.7 (1.0-11.4)
N3	H3p1	24.8 (22.0-26.9)	9.3 (5.2-15.5)	7.9 (3.1-12.3)	2.9 (0.7-9.6)
N3	H3p2	13.3 (9.5-15.1)	8.0 (3.3-12.0)	5.9 (2.7-10.9)	0.0 (0.0-5.5)
N6	H1p1	14.0 (12.9-15.2)	5.2 (0.6-12.0)	1.1 (0.0-5.6)	0.0 (0.0-0.0)
N6	H1p2	17.0 (12.8-20.2)	7.4 (3.3-11.7)	0.0 (0.0-10.3)	0.0 (0.0-3.3)
N6	H1	19.9 (18.4-21.6)	5.6 (2.6-9.9)	4.8 (0.0-8.1)	0.0 (0.0-1.8)
N6	H3p1	19.1 (15.7-21.7)	7.7 (0.5-17.0)	7.7 (1.6-14.0)	2.9 (0.4-9.9)
N6	H3p2	16.1 (12.9-19.4)	6.8 (0.5-16.1)	6.3 (0.3-15.8)	2.5 (0.1-14.9)
N6	H3	17.2 (14.2-19.0)	6.0 (0.5-15.4)	7.7 (1.9-17.0)	3.4 (0.8-10.6)
	All	18.2 (16.3-20.6)	7.6 (6.2-9.0)	7.0 (5.1-7.8)	2.7 (0.0-3.3)

Table D4 Descriptive statistics of voltage (peak-to-peak amplitude) measured in milliVolts (mV). Location H2 was used to analyze if there is an effect of a conduction gap in the ablation line on the voltage. During the first and second lesion a piece of rubber was present on the ablation clamp to create an artificial gap in the conduction line. An area of 64 electrodes around the ablation lesion, 32 cm on the proximal and 32 on the distal side, was included in this analysis.

		Median (IQR)			
Subject	Location	Baseline	Lesion 1	Lesion 2	Lesion 3
N2	H2p1	14.8 (13.9-18.8)	8.8 (2.4-12.2)	5.2 (3.3-6.8)	3.7 (2.0-6.1)
N2	H2p2	19.1 (17.1-19.9)	9.3 (2.7-11.9)	7.8 (2.6-11.3)	3.5 (1.1-6.6)
N3	H2p1	18.6 (16.6-21.0)	12.4 (5.9-19.5)	9.8 (3.8-18.0)	3.1 (0.0-5.8)
N3	H2p2	14.3 (13.1-15.8)	8.4 (3.8-14.7)	7.9 (4.8-19.3)	4.9 (0.1-7.8)
N6	H2p1	22.6 (19.1-26.5)	10.7 (4.1-17.0)	6.6 (0.0-14.7)	1.3 (0.0-6.5)
N6	H2p2	12.8 (11.0-16.8)	10.5 (4.3-16.4)	6.5 (0.1-12.0)	0.3 (0.0-8.2)
N6	H2	24.1 (21.1-26.9)	12.3 (4.7-20.2)	10.6 (2.7-21.1)	1.6 (0.0-6.3)
	All	18.6 (14.6-20.8)	10.5 (9.0-11.5)	7.8 (6.6-8.9)	3.1 (1.5-3.6)

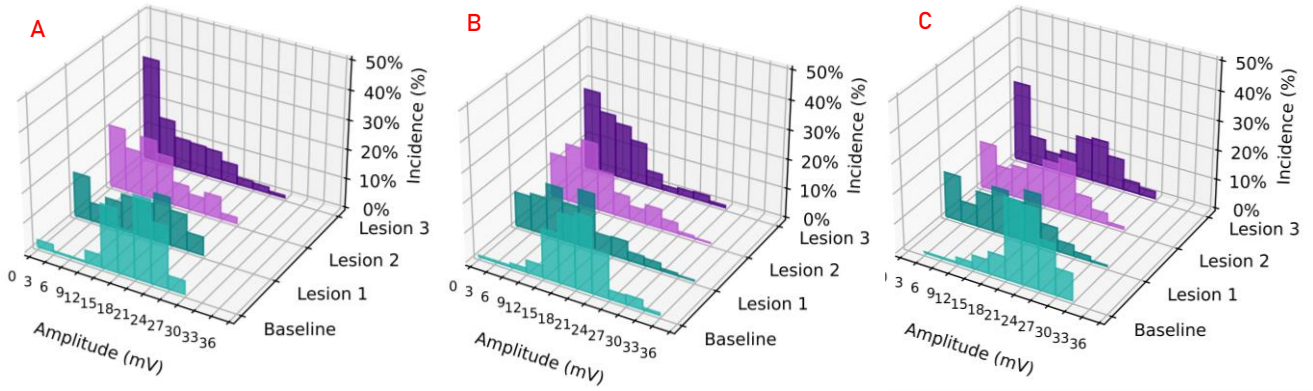

Figure D1 Histograms of the relative frequency distribution of median amplitudes (per electrode over the different waves) over the different lesion stages. These amplitude were recorded during pacing from location 1, in mapping locations A) H1; B) H2; C) H3. Subjects N3, and N6 are combined in the histograms of location H1 (A) and H3 (C). Subjects N2, N3, and N6 are combined in the histogram of location H2 (B).

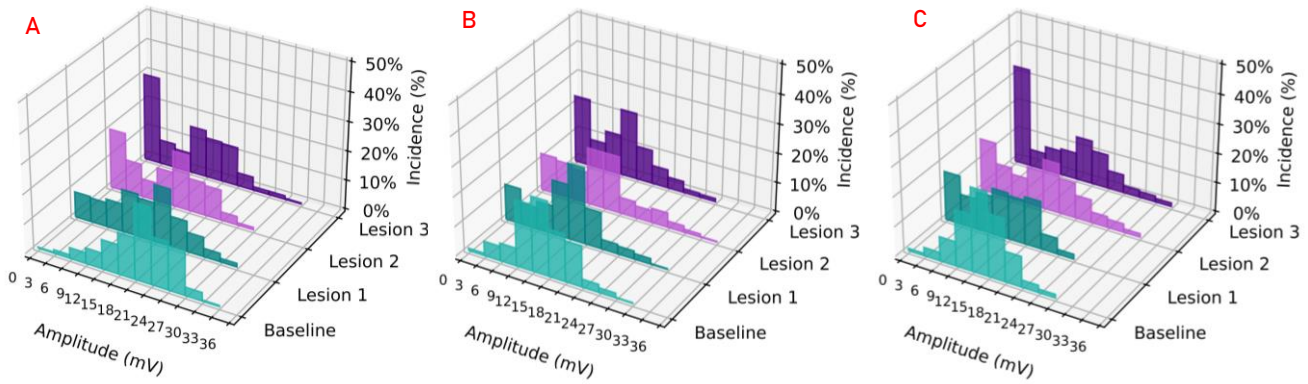

Figure D2 Histograms of the relative frequency distribution of median amplitudes (per electrode over the different waves) over the different lesion stages. These amplitude were recorded during pacing from location 2, in mapping locations A) H1; B) H2; C) H3. Subjects N3, and N6 are combined in the histograms of location H1 (A) and H3 (C). Subjects N2, N3, and N6 are combined in the histogram of location H2 (B).

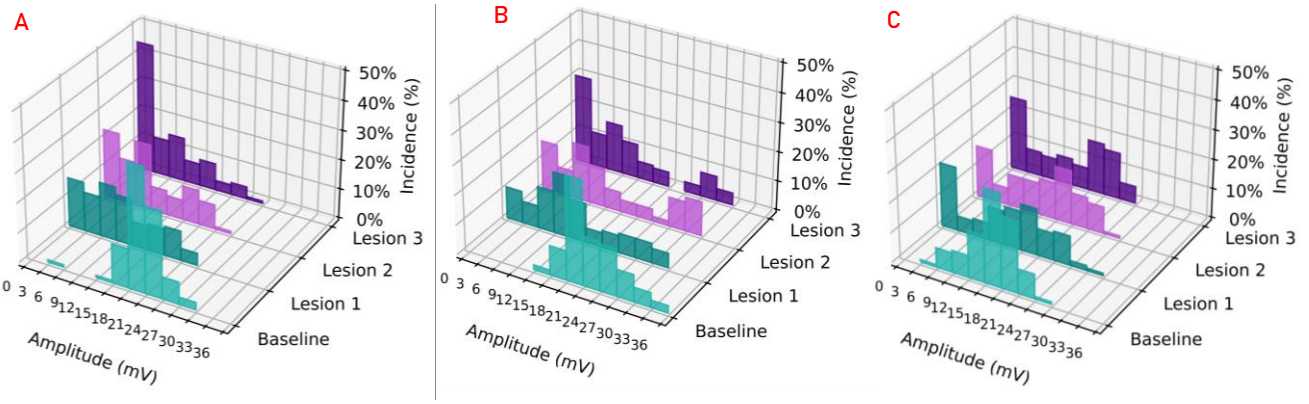

Figure D3 Histogram of the relative frequency distribution of median amplitudes (per electrode over the different waves) over the different lesion stages. These amplitude were recorded during intrinsic rhythm, in mapping locations A) H1; B) H2; C) H3. Intrinsic rhythm was only measured in subject N6.

Potential slope

Table D5 Descriptive statistics of slope (Volt/second). Locatios H1 and H3 were used to analyze the difference in slope between different stages of ablation lesions. An area of 64 electrodes around the ablation lesion, 32 on the proximal and 32 on the distal side, was included in this analysis.

		Median (IQR)			
Subject	Location	Baseline	Lesion 1	Lesion 2	Lesion 3
N3	H1p1	-2.0 (-2.7--1.3)	-1.8 (-2.7--0.9)	-1.0 (-1.7--0.4)	-0.4 (-1.0--0.2)
N3	H1p2	-2.4 (-3.1--1.4)	-1.2 (-3.1--0.6)	-1.1 (-2.6--0.3)	-0.3 (-1.8--0.1)
N3	H3p1	-1.8 (-2.3--1.4)	-0.7 (-1.5--0.4)	-0.5 (-1.3--0.3)	-0.2 (-0.9--0.1)
N3	H3p2	-1.0 (-1.6--0.7)	-0.5 (-1.0--0.2)	-0.5 (-1.2--0.3)	0.0 (-0.5-0.0)
N6	H1p1	-0.7 (-1.4--0.4)	-0.3 (-1.0--0.0)	-0.1 (-0.3-0.0)	0.0 (0.0-0.0)
N6	H1p2	-1.4 (-1.7--1.0)	-0.3 (-0.7--0.2)	0.0 (-0.5-0.0)	0.0 (-0.2-0.0)
N6	H1	-1.6 (-2.0--1.4)	-0.5 (-1.2--0.2)	-0.4 (-0.6-0.0)	0.0 (-0.2-0.0)
N6	H3p1	-1.5 (-2.0--1.1)	-0.4 (-1.5--0.1)	-0.6 (-1.9--0.2)	-0.3 (-1.3--0.1)
N6	H3p2	-1.7 (-2.8--1.4)	-0.5 (-1.4--0.1)	-0.6 (-2.2--0.1)	-0.3 (-1.7--0.0)
N6	H3	-2.5 (-2.8--2.0)	-0.8 (-1.9--0.1)	-1.6 (-3.1--0.3)	-0.5 (-1.6--0.1)
	All	-1.6 (-2.0--1.4)	-0.5 (-0.8--0.4)	-0.6 (-0.9--0.4)	-0.2 (-0.3-0.0)

Table D6 Descriptive statistics of slope (volt/second). Location H2 was used to analyze if there is an effect of a conduction gap in the ablation line on the slope. During the first and second lesion a piece of rubber was present on the ablation clamp to create an artificial gap in the conduction line. An area of 64 electrodes around the ablation lesion, 32 on the proximal and 32 on the distal side, was included in this analysis.

		Median (IQR)			
Subject	Location	Baseline	Lesion 1	Lesion 2	Lesion 3
N2	H2p1	-1.3 (-1.5--0.9)	-0.4 (-0.6--0.2)	-0.4 (-0.6--0.2)	-0.3 (-0.5--0.2)
N2	H2p2	-1.8 (-2.0--1.6)	-0.4 (-0.9--0.2)	-0.4 (-1.0--0.3)	-0.2 (-0.6--0.1)
N3	H2p1	-1.0 (-1.3--0.7)	-1.3 (-3.0--0.4)	-1.1 (-2.7--0.4)	-0.2 (-0.4-0.0)
N3	H2p2	-1.0 (-2.5--0.7)	-0.8 (-1.8--0.3)	-1.3 (-3.1--0.3)	-0.3 (-0.5--0.0)
N6	H2p1	-1.9 (-2.6--1.3)	-0.6 (-1.1--0.2)	-0.8 (-1.6-0.0)	-0.1 (-0.5-0.0)
N6	H2p2	-1.3 (-1.8--0.8)	-0.6 (-1.6--0.3)	-0.5 (-1.4--0.0)	-0.1 (-0.5-0.0)
N6	H2	-2.7 (-3.1--2.4)	-1.4 (-2.6--0.5)	-1.7 (-2.8--0.3)	-0.2 (-0.7-0.0)
	All	-1.3 (-1.8--1.2)	-0.6 (-1.0--0.5)	-0.8 (-1.2--0.4)	-0.2 (-0.2--0.2)

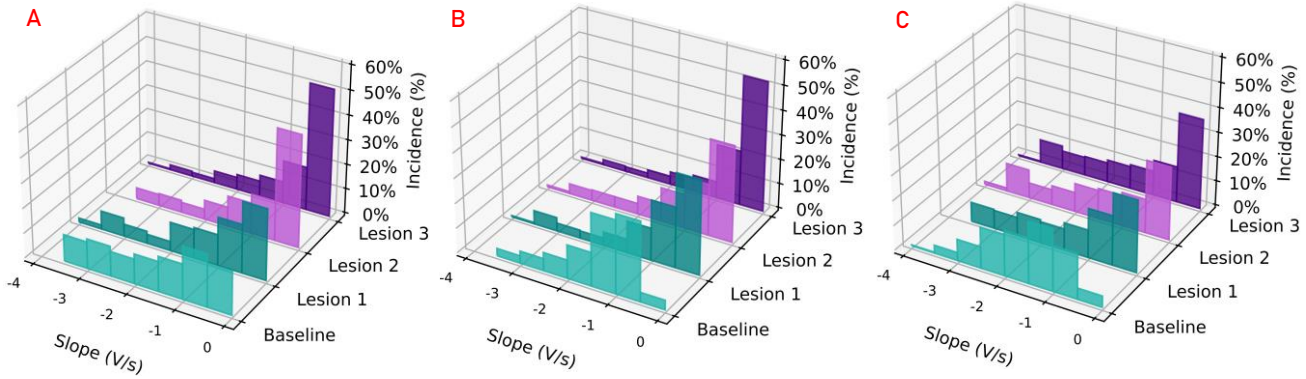

Figure D4 Histograms of the relative frequency distribution of slopes (V/s) over the different lesion stages during pacing from location 1, in mapping locations A) H1; B) H2; C) H3. Subjects N3, and N6 are combined in the histograms of location H1 (A) and H3 (C). Subjects N2, N3, and N6 are combined in the histogram of location H2 (B).

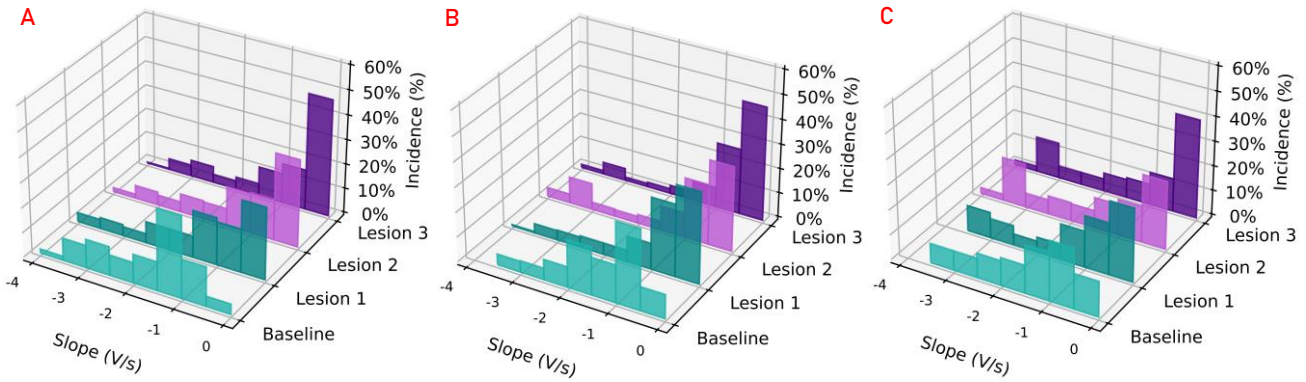

Figure D5 Histograms of the relative frequency distribution of slopes (V/s) over the different lesion stages during pacing from location 2, in mapping locations A) H1; B) H2; C) H3. Subjects N3, and N6 are combined in the histograms of location H1 (A) and H3 (C). Subjects N2, N3, and N6 are combined in the histogram of location H2 (B).

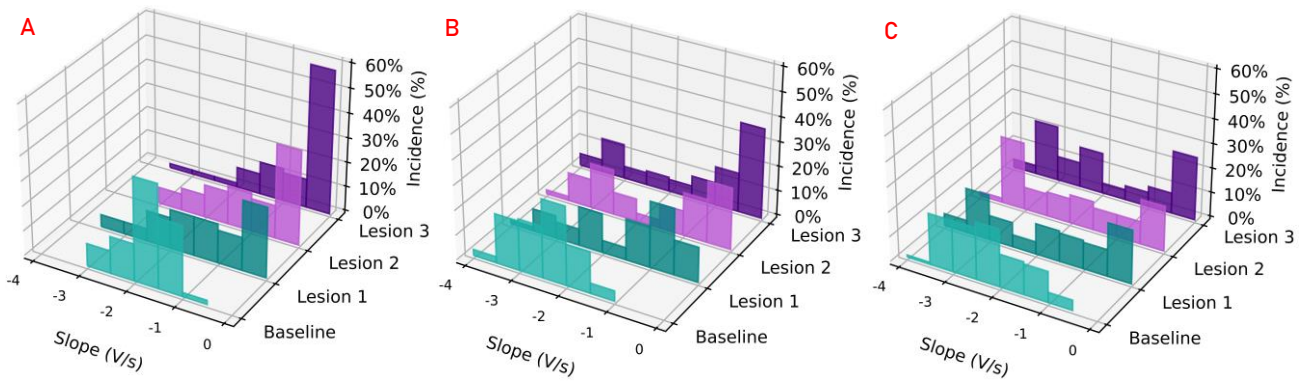

Figure D6 Histogram of the relative frequency distribution of median slopes (V/s) (per electrode over the different waves) over the different lesion stages. These amplitude were recorded during intrinsic rhythm, in mapping locations A) H1; B) H2; C) H3. Intrinsic rhythm was only measured in subject N6.

R/S ratio

Table D7 Descriptive statistics of R- to S-amplitude ratio (R/S ratio). Locations H1 and H3 were used to analyze the difference in voltage between different stages of ablation lesions. An area of 64 electrodes around the ablation lesion, 32 on the proximal and 32 on the distal side, was included in this analysis.

		Median (IQR)			
Subject	Location	Baseline	Lesion 1	Lesion 2	Lesion 3
N3	H1p1	0.6 (0.3-0.7)	0.1 (-0.4-0.3)	0.2 (0.0-0.6)	0.2 (-0.3-0.5)
N3	H1p2	0.8 (0.7-0.8)	0.3 (-0.1-0.6)	0.4 (0.1-0.6)	0.0 (-0.6-0.7)
N3	H3p1	0.7 (0.5-0.7)	0.1 (-0.3-0.5)	0.3 (-0.3-0.6)	-0.3 (-0.8-0.2)
N3	H3p2	0.7 (0.5-0.8)	0.8 (0.3-0.8)	0.5 (-0.2-0.8)	0.6 (-0.8-0.8)
N6	H1p1	0.6 (0.4-0.7)	0.7 (0.4-0.8)	0.7 (-0.1-0.9)	0.1 (-0.7-0.8)
N6	H1p2	0.6 (0.5-0.7)	0.5 (-0.3-0.6)	0.7 (0.4-0.9)	0.3 (-0.3-0.6)
N6	H1	0.7 (0.6-0.8)	0.5 (0.3-0.7)	0.1 (-0.9-0.6)	0.3 (-0.4-0.7)
N6	H3p1	0.6 (0.5-0.7)	0.3 (-0.1-0.5)	0.0 (-0.5-0.4)	-0.2 (-0.8-0.4)
N6	H3p2	0.4 (0.2-0.7)	-0.3 (-0.8-0.5)	-0.0 (-0.7-0.6)	-0.6 (-0.9-0.1)
N6	H3	0.4 (0.2-0.6)	0.1 (-0.5-0.6)	0.2 (-0.2-0.6)	-0.0 (-0.5-0.4)
	All	0.6 (0.6-0.7)	0.3 (0.1-0.5)	0.2 (0.1-0.5)	0.0 (-0.2-0.3)

Table D8 Descriptive statistics of R- to S-amplitude ratio. Locations H2 was used to analyze if there is an effect of a conduction gap in the ablation line on the voltage. During the first and second lesion a piece of rubber was present on the ablation clamp to create an artificial gap in the conduction line. An area of 64 electrodes around the ablation lesion, 32 on the proximal and 32 on the distal side, was included in this analysis.

		Median (IQR)			
Subject	Location	Baseline	Lesion 1	Lesion 2	Lesion 3
N2	H2p1	0.7 (0.6-0.9)	0.8 (0.5-0.9)	0.7 (0.6-0.9)	-0.1 (-0.6-0.5)
N2	H2p2	0.7 (0.6-0.7)	0.3 (-0.4-0.6)	0.6 (-0.4-0.9)	-0.0 (-0.3-0.4)
N3	H2p1	0.8 (0.6-0.8)	0.3 (-0.3-0.7)	0.5 (0.2-0.7)	0.1 (-0.5-0.6)
N3	H2p2	0.8 (0.6-0.9)	0.4 (-0.2-0.7)	0.2 (-0.2-0.5)	0.4 (-0.5-0.8)
N6	H2p1	0.7 (0.6-0.8)	0.5 (0.2-0.7)	0.2 (-0.2-0.7)	-0.3 (-0.8-0.3)
N6	H2p2	0.6 (0.2-0.9)	0.2 (-0.2-0.7)	-0.2 (-0.6-0.5)	-0.7 (-1.0-0.0)
N6	H2	0.6 (0.5-0.6)	-0.2 (-0.5-0.3)	0.4 (-0.3-0.6)	-0.6 (-0.9--0.1)
	All	0.7 (0.6-0.8)	0.3 (0.2-0.4)	0.4 (0.2-0.6)	-0.1 (-0.4-0.0)